Bioactive Materials 26 (2023) 337–352

Contents lists available at ScienceDirect

Bioactive Materials

journal homepage: www.keaipublishing.com/en/journals/bioactive-materials

Engineered macrophage-biomimetic versatile nanoantidotes for inflammation-targeted therapy against Alzheimer's disease by neurotoxin neutralization and immune recognition suppression

Meng Cheng [a,1], Caihua Ye [a,1], Chunxiao Tian [b,1], Dongju Zhao [c], Haonan Li [a], Zuhao Sun [a], Yuyang Miao [d], Qiang Zhang [d,***], Junping Wang [a,**], Yan Dou [a,*]

[a] Department of Radiology and Tianjin Key Laboratory of Functional Imaging, Tianjin Medical University General Hospital, Tianjin, 300052, PR China
[b] School of Biomedical Engineering and Technology, Tianjin Medical University, Tianjin, 300070, PR China
[c] School of Life Sciences, Tianjin University, Tianjin, 300072, PR China
[d] Department of Geriatrics, Tianjin Medical University General Hospital, Tianjin Geriatrics Institute, Tianjin, 300052, PR China

ARTICLE INFO

Keywords:
Alzheimer's disease
Biomimetic nanomedicine
Biological neutralization
Immune recognition and response
Neuroinflammation-targeted therapy
9.4T MR imaging

ABSTRACT

Immune recognition of excessive neurotoxins by microglia is a trigger for the onset of neuroinflammation in the brain, leading to neurodegeneration in Alzheimer's disease (AD). Blocking active recognition of microglia while removing neurotoxins holds promise for fundamentally alleviating neurotoxin-induced immune responses, but is very challenging. Herein, an engineered macrophage-biomimetic versatile nanoantidote (OT-Lipo@M) is developed for inflammation-targeted therapy against AD by neurotoxin neutralization and immune recognition suppression. Coating macrophage membranes can not only endow OT-Lipo@M with anti-phagocytic and inflammation-tropism capabilities to target inflammatory lesions in AD brain, but also efficiently reduce neurotoxin levels to prevent them from activating microglia. The loaded oxytocin (OT) can be slowly released to downregulate the expression of immune recognition site Toll-like receptor 4 (TLR4) on microglia, inhibiting TLR4-mediated pro-inflammatory signalling cascade. Benefiting from this two-pronged immunosuppressive strategy, OT-Lipo@M exhibits outstanding therapeutic effects on ameliorating cognitive deficits, inhibiting neuronal apoptosis, and enhancing synaptic plasticity in AD mice, accompanied by the delayed hippocampal atrophy and brain microstructural disruption by *in vivo* 9.4T MR imaging. This work provides new insights into potential AD therapeutics targeting microglia-mediated neuroinflammation at the source.

1. Introduction

Microglia-mediated neuroinflammation is considered a key inducer of progressive neurodegeneration in Alzheimer's disease (AD) [1,2]. As primary resident immune cells in the central nervous system (CNS), microglia maintain brain microenvironment homeostasis by triggering innate immune responses [3]. In AD brain, excessive neurotoxins such as lipopolysaccharide (LPS) and amyloid-beta (Aβ) aggregates bind to pattern recognition receptors (PRRs) on microglial membranes as pathogen-associated molecular patterns (PAMPs) or damage-associated molecular patterns (DAMPs), resulting in sustained microglial activation and long-term release of inflammatory mediators, ultimately leading to synaptic damage and neuronal dysfunction [4,5]. It is worth noting that the deleterious inflammatory phenotype of microglia during AD progression depends on the specific immune recognition of neurotoxins by PRRs, which is increasingly recognized as a trigger for the onset of microglia-mediated pro-inflammatory cascade. Therefore, reducing neurotoxin levels while attenuating PRR expression is highly desirable and challenging for alleviating neurotoxin-induced immune responses and neuroinflammation in AD.

Peer review under responsibility of KeAi Communications Co., Ltd.
* Corresponding author.
** Corresponding author.
*** Corresponding author.
E-mail addresses: zhangqiangyulv@163.com (Q. Zhang), wangjunping_tj@163.com (J. Wang), douyan@tmu.edu.cn (Y. Dou).
[1] These authors contributed equally to this work.

https://doi.org/10.1016/j.bioactmat.2023.03.004
Received 27 October 2022; Received in revised form 21 February 2023; Accepted 6 March 2023

Cell-membrane biomimetic nanomaterials have attracted much attention, masquerading as "decoys" to intercept virulent factors and divert them away from their intended cellular targets, thereby achieving biological neutralization to reduce toxin levels, especially suitable for broad-spectrum detoxification [6,7]. As effector cells of immune defense, the membranes of macrophages are colonized with a large number of PRRs, which have been reported to neutralize endotoxins to suppress inflammation in sepsis and hepatic ischemia-reperfusion [8,9], but their effect on neutralizing neurotoxins in AD has not been proven. Furthermore, macrophage-biomimetic nanocarriers also inherit the low immunogenicity of source cells and the natural advantage of being recruited to inflammatory lesions [10–12], which is expected to enable targeted delivery to neuroinflammatory areas in AD brain where neurotoxins accumulate, thereby optimizing biological neutralization and loaded drug efficacy. Biomimetic nanocarriers with inflammation-tropism capability have been developed for drug delivery therapy in atherosclerosis or acute ischemic stroke [13,14], but their application in AD treatment has not been investigated. Therefore, utilizing macrophage-biomimetic nanoagents to simultaneously exert inflammation-tropism and neurotoxin neutralization is an emerging therapeutic strategy focusing on neurodetoxification in CNS diseases such as AD.

Evidence exists that Toll-like receptor 4 (TLR4) is the most common type of PRRs and its expression is prominently high in AD brain, providing sufficient binding sites for microglia to recognize neurotoxins [15,16]. The binding of TLR4 to neurotoxins triggers the myeloid differentiation factor 88 (Myd88)-dependent signalling pathways that exacerbate the transcriptional expression of various inflammatory cytokines [17]. The resulting exacerbation of microglial activation further upregulates TLR4 expression and promotes its dependent immune recognition of neurotoxins, leading to a vicious circle of inflammatory cascade [18,19]. Oxytocin (OT), a neuroendocrine hormone, has been shown to attenuate microglial overactivation and neuroinflammation [20,21], but its specific regulatory mechanisms in the CNS has not been fully elucidated. Previous studies have shown that exogenous OT can inhibit TLR4 expression and block its downstream inflammatory signalling pathways to mitigate bone cancer pain, maternal separation stress, and lung injury [22–24], but whether it can play a similar role in AD brain remains unclear. Therefore, attenuating TLR4 expression and its mediated pro-inflammatory cascade by exogenous OT is of great value and exploratory significance for suppressing microglia-mediated immune recognition of neurotoxins in AD.

Herein, OT-loaded macrophage-biomimetic liposomes were engineered as a versatile nanoantidote (OT-Lipo@M) for inflammation-targeted therapy against AD by neurotoxin neutralization and immune recognition suppression (Scheme 1). Coating macrophage membranes not only endowed OT-Lipo@M with anti-phagocytic and inflammation-tropism capabilities, greatly enhancing the preferential delivery to inflammatory lesions in AD brain, but also served as a "nanodecoy" for efficient removal of neurotoxins. Furthermore, the OT released from OT-Lipo@M could reduce TLR4 expression on microglia, synergistically inhibiting TLR4-mediated pro-inflammatory signalling cascade. As a result, based on this two-pronged immunosuppressive strategy, OT-Lipo@M administration exhibited outstanding therapeutic effects on ameliorating cognitive deficits, inhibiting neuronal apoptosis, and enhancing synaptic plasticity in AD mice, accompanied by the delayed hippocampal atrophy and brain microstructural disruption by *in vivo* 9.4T MR imaging. To our knowledge, this work is the first report on developing a multifunctional biomimetic nanomedicine for AD that simultaneously possesses inflammation-tropism, neurotoxin neutralization, and immune recognition suppression to comprehensively, efficiently, and safely block the trigger source of microglia-mediated neuroinflammation.

2. Materials and methods

2.1. Materials, cells, and animals

1,2-distearoyl-*sn*-glycero-3-phosphoethanolamine-N-PEG2000 (DSPE-PEG2000) was purchased from Macklin (Shanghai, China). 1,2-dipalmitoyl-*sn*-glycero-3-phosphocholine (DPPC) was purchased from Aladdin (Shanghai, China). Cholesterol and lipopolysaccharides (LPS, *Escherichia coli* O127:B8, L3129) were purchased from Sigma-Aldrich (USA). Oxytocin acetate was purchased from MedChemExpress (USA). Membrane and Cytosol Protein Extraction Kit and Coomassie Blue Fast Staining Solution were purchased from Beyotime Biotechnology

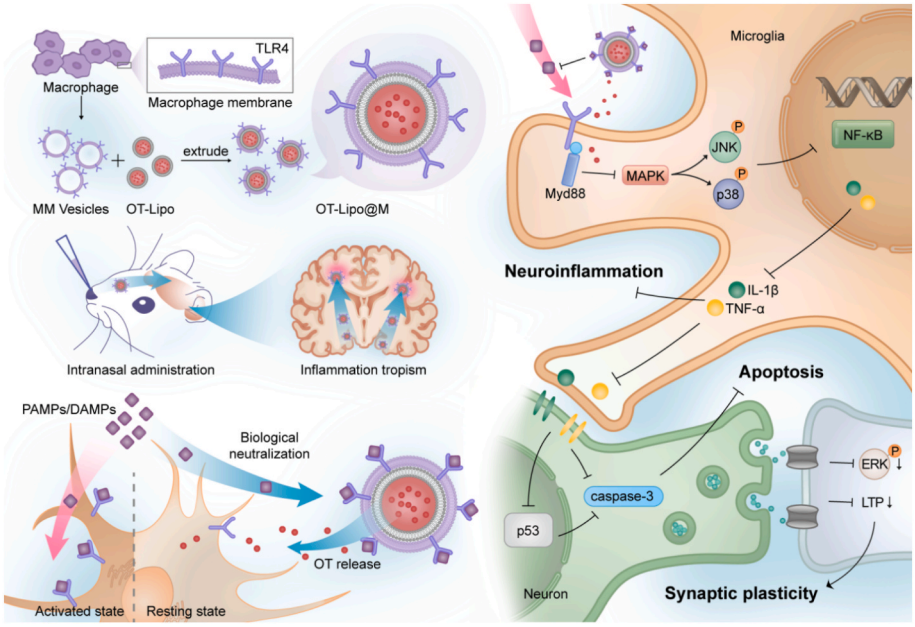

Scheme 1. Schematic illustration of the engineered macrophage-biomimetic versatile nanoantidote OT-Lipo@M and its anti-AD mechanisms, including inflammation-targeted delivery, neurotoxin neutralization, and immune recognition suppression, thereby inhibiting microglia-mediated pro-inflammatory cascade to alleviate neurodegeneration.

(Shanghai, China). LPS ELISA kit was purchased from Cloud-Clone Corp (Wuhan, China). The mouse TNF-α ELISA kit and IL-1β ELISA kit were purchased from NeoBioscience Technology (Shenzhen, China). The Annexin V-FITC/PI assay kit was purchased from KeyGen Biotech (Nanjing, China). The Reactive Oxygen Species (ROS) assay kit was purchased from Solarbio (Beijing, China).

RAW 264.7 cells, BV-2 cells and HT22 cells were cultured in high glucose Dulbecco's modified Eagle's medium (DMEM) supplemented with 10% fetal bovine serum (FBS) and 1% penicillin/streptomycin (P/S) in an incubator with 5% CO_2 at 37 °C. C57BL/6J mice and APP/PS1 mice were purchased from Beijing HFK Bioscience Co. Ltd. All animal experiments were performed in accordance with the guidelines approved by the Animal Care and Use Committee of the Institute of Radiation Medicine, Chinese Academy of Medical Sciences (SYXK2019-0002).

2.2. Macrophage membrane extraction and their vesicles preparation

Macrophage membranes were isolated from RAW 264.7 cells using a membrane protein extraction kit according to the reported method [25]. Briefly, RAW 264.7 cells were harvested and washed with PBS by centrifugation, and then suspended in the membrane protein extraction reagent A (adding 1 mM PMSF before use) and cooled down in an ice bath for 15 min. Then, cells were destroyed more than 50 times with a pre-cooled glass homogenizer, and the resulting solution was separated by centrifugation at 700×*g* for 10 min at 4 °C, then the membranes were obtained by centrifugation at 14,000×*g* for 30 min at 4 °C. Cell membrane precipitation from 2.5 × 10^7 cells was suspended with 1 mL deionized water and extruded sequentially through 400 nm and 200 nm pore-size polycarbonate filters to prepare macrophage membrane vesicles using an Avanti mini extruder (Avanti Polar Lipids, USA).

2.3. Fabrication of OT-Lipo and OT-Lipo@M

The liposomes were prepared by the thin-film hydration method according to previous reports [26,27]. In detail, 80 μmol lipid compositions of DPPC/Cholesterol/DSPE-PEG2000 (6:3:1, molar ratio) were dissolved in 4 mL chloroform/methanol (3:1, volume ratio). After evaporated in a rotavapor for 20 min at 60 °C, the formed lipid films were dried under vacuum for 12 h and hydrated at 50 °C with 4 mL OT solution (1 mg/mL) to obtain liposomes. 4 mL OT solution containing 20 μL DiO (Beyotime, C1993S) or DiL (Beyotime, C1991S) was used for hydration to prepare DiO-labeled or DiL-labeled liposomes. Liposomes were then extruded 10 times through 400 nm, 200 nm and 100 nm pore-size polycarbonate filters at 45 °C. OT-Lipo@M was fabricated by coating OT-Lipo with macrophage membranes by a direct extrusion method [28]. Briefly, macrophage membrane vesicles prepared above were mixed with 1 mL of OT-Lipo, and extruded sequentially through 400 nm and 200 nm pore-size polycarbonate filters. The final OT-Lipo@M was purified by centrifugation (16,000×*g*, 20 min, 4 °C) to remove excess free membranes. The unloaded OT was removed by high-speed centrifugation (Avanti J-26XP, Beckman, USA) at 40,000×*g* for 1 h at 4 °C to obtain OT-Lipo or OT-Lipo@M.

2.4. Characterization

The particle size and zeta potential were measured with dynamic light scattering instrument (Nano-ZS90 zetasizer, Malvern, UK), and the particle morphology was observed using transmission electron microscopy (HT7700, HITACHI, Japan) after negative staining with 2% phosphotungstic acid solution. UV–vis spectra of OT and liposomes were recorded with a spectrophotometer (UV-3600 Plus, SHIMADZU, Japan). To detect the protein profiles, samples were separated on a 12.5% SDS-PAGE gel by a Mini-PROTEAN Tetra System (Bio-Rad, CA, USA), subsequently stained with Coomassie blue and visualized after destaining with water. To verify the successful combination of OT-Lipo with macrophage membranes, OT-Lipo and macrophage membranes were respectively labeled with DiL and DiO according to previous reports [29]. Dual-color fluorescein-labeled OT-Lipo@M was then prepared by co-extrusion and incubated with BV-2 cells for 6 h. After staining the nuclei with DAPI, the colocalization of red (DiL) and green (DiO) fluorescence was observed under a laser confocal microscope (A1 HD25, Nikon, Japan).

2.5. EE, LC, and in vitro release of OT

The standard curve of UV–vis absorption of OT with different concentrations was plotted based on the characteristic absorption of OT at 275 nm. Then, 0.5 mL of OT-Lipo or OT-Lipo@M were mixed with 2.5 mL of methanol and sonicated to demulsify the composite liposomes. The encapsulation efficiency (EE%) and the loading capacity (LC%) of OT in OT-Lipo and OT-Lipo@M were calculated using the following equations:

$$EE\% = \frac{\text{the amount of loaded OT}}{\text{the amount of total OT}} \times 100\%$$

$$LC\% = \frac{\text{the amount of loaded OT}}{\text{the amount of liposomes}} \times 100\%$$

For detecting *in vitro* OT release, dialysis bags (MW. Cutoff: 3.5 kDa) containing 1 mL of OT-Lipo or OT-Lipo@M were directly immersed in PBS (pH = 7.4) and shaken continuously at 100 rpm at 37 °C. At the indicated time points, the amount of OT released was measured using UV–vis spectrophotometry according to the standard curve.

2.6. In vitro neutralization of LPS by OT-Lipo@M

LPS solution (7.5 ng/mL) was mixed with the same volume of OT-Lipo and OT-Lipo@M, respectively, and then incubated at 37 °C for 2 h. The supernatant was collected by centrifugation to remove liposomes, and ELISA was performed and the optical density was measured at 450 nm with a multi-mode microplate reader to detect the amount of remaining LPS. PBS was used as the negative control.

2.7. Cellular uptake

To assess the antiphagocytic effect of OT-Lipo@M *in vitro*, RAW 264.7 cells were used as a classical *in vitro* model of macrophages for cellular uptake according to previous reports [13,30]. Briefly, RAW 264.7 cells were seeded in 24-well plates at a density of 4 × 10^5 cells/well for 24 h and then incubated with DiO-labeled OT-Lipo and OT-Lipo@M for 4 h, respectively. To assess the inflammation-tropism ability of OT-Lipo@M *in vitro*, BV-2 cells were treated with LPS (100 μg/mL) for 12 h to mimic the cellular inflammatory microenviroment and then incubated with DiO-labeled OT-Lipo and OT-Lipo@M for 1 h. After staining nuclei with DAPI, cells were observed under a confocal laser scanning microscope (A1 HD25, Nikon, Japan). Meanwhile, the fluorescence intensity of cells was quantified by flow cytometer (BD Accuri™ C6 PlusFlow Cytometer, BD, USA).

2.8. Cell viability assay

BV-2 cells and HT22 cells were cultured in 96-well plates at a density of 3 × 10^4 cells/well at 37 °C incubator for 24 h. To assess the cytotoxicity of liposomes, cells were respectively incubated with OT-Lipo or OT-Lipo@M containing OT concentration of 3, 12, 24, and 30 μg/mL for 24 h and 48 h, respectively. To assess the effect of liposomes on LPS-stimulated cell viability, cells were pre-incubated with LPS (100 μg/mL) for 12 h and then treated with OT-Lipo or OT-Lipo@M containing OT concentration of 6, 12, and 18 μg/mL for 24 h. Then, 10 μL CCK-8 was added and the absorbance were detected after 2 h at 450 nm with a multi-mode microplate reader (BioTek SYNERGY HTX, USA).

2.9. Cell immunofluorescence imaging and ELISA assay

BV-2 cells were cultured in 12-well plates at a density of 2×10^5 cells/well for 24 h and then treated with LPS (100 μg/mL) for 12 h, followed by OT-Lipo, OT-Lipo@M (containing OT concentration of 12 μg/mL) and Lipo@M incubation for 24 h. After washing with PBS three times, cells were fixed in 4% paraformaldehyde (PFA) for 15 min, permeabilized with Triton X-100 for 10 min, and blocked with 5% Bovine Serum Albumin (BSA) for 45 min at 37 °C. Cells were incubated overnight at 4 °C with the following primary antibodies: Iba-1 (1:300, Abcam) and TLR4 (1:200, Affinity). After washing with PBS three times, cells were incubated with the appropriate fluorescent-conjugated secondary antibody (1:200, Zhongshan Jinqiao) for 1 h at 37 °C. Cells were then stained with DAPI and observed using an inverted fluorescence microscope (IX73, OLYMPUS, Japan). Images were analyzed using ImageJ software. In addition, the levels of TNF-α and IL-1β in the supernatant of BV-2 cells after various treatments were measured by ELISA assay.

2.10. BV-2 cell-conditioned media-induced neurotoxicity

BV-2 cells and HT22 cells were cultured in 96-well plates (3×10^4 cells/well) for 24 h, respectively. BV-2 cells were treated with LPS (100 μg/mL) for 12 h, followed by OT-Lipo or OT-Lipo@M containing OT concentration of 6, 12, and 18 μg/mL incubation for 24 h. Then, BV-2 cell-conditioned media (CM) was applied to treat HT22 cells for another 24 h. CCK-8 assay was performed to evaluate cell viability of HT22 cells.

BV-2 cells and HT22 cells were cultured in 24-well plates (1×10^5 cells/well) respectively. BV-2 cells were treated with LPS (100 μg/mL) for 12 h, followed by OT-Lipo or OT-Lipo@M containing OT concentration of 12 μg/mL incubation for 24 h. Then, BV-2 CM was applied to treat HT22 cells for another 24 h. The apoptosis of HT22 cells was detected by flow cytometer using the Annexin V-FITC/PI apoptosis detection kit according to the manufacturer's instructions.

2.11. Brain-targeted, biodistribution and pharmacokinetics studies

C57BL/6J mice (female, 8-week-old) were intranasally administrated by DiL-labeled OT-Lipo and OT-Lipo@M, respectively, and visualized under an *in vivo* fluorescence imaging system (IVIS® Lumina LT III , PerkinElmer) at 10 min, 1 h, 8.5 h, 24 h, and 48 h after administration. Meanwhile, the heart, liver, spleen, lung, kidney, and brain were rapidly harvested for *ex vivo* fluorescence imaging at above indicated time points. Brain was harvested at 24 h after administration and prepared into 20 μm cryosections on a Leica CM1950 cryostat (Germany). After stained with DAPI, the images were obtained using Pannoramic digital scanners (3D HISTECH, Hungary). To define plasma pharmacokinetics of OT-Lipo and OT-Lipo@M, blood samples were collected at indicated time points (10 min, 1 h, 2 h, 4 h, 6 h, 8.5 h, 24 h, 48 h, 72 h, 96 h and 120 h) after administration. The plasma was obtained by centrifugation at 3000 rpm for 10 min, and diluted 1:100 with PBS prior to fluorescence measurements. The fluorescence intensity was detected using a fluorespectro photometer (F-7000, Hitachi, Japan).

2.12. Intracerebral inflammation-tropism studies

To induce the local inflammation in the hippocampus, the modeling protocol based on stereotactic injection of LPS was modified according to previous reports [31]. In detail, C57BL/6J mice (male, 24-week-old) were kept under anesthesia and positioned in a stereotactic head frame. Then, 4 μL 25 μg/μL LPS (Solarbio, *Escherichia coli* 055:B5, L8880) was stereotaxically injected at a constant rate of 200 nL/min into the right hippocampus (2.0 mm posterior to the bregma, 1.5 mm right from the midline, and 1.5 mm ventral). PBS injection was performed as the sham group. Four days later, the mice were intranasally administrated by DiL-labeled OT-Lipo and OT-Lipo@M, and then the brain was harvested after administration. The sections were incubated with anti-Iba-1 (1:300, Abcam) and anti-CD68 (1:200, Boster) overnight at 4 °C. The sections were incubated with FITC-conjugated goat anti-rabbit secondary antibody (1:200, Sungene Biotech) for 1 h at room temperature. Images were obtained under a confocal fluorescence microscope (A1 HD25, Nikon, Japan). The fluorescence intensities of DiL, Iba-1, and CD68 were analyzed and the colocalization of DiL with Iba-1 or CD68 was calculated using Manders' overlap coefficient by ImageJ software.

2.13. In vivo administration

C57BL/6J mice (female, 24-week-old, n = 15) were intranasally administrated with 30 μL saline as the WT group. APP/PS1 mice (female, 24-week-old) were randomly divided into three groups (n = 15 per group) and given the following intranasal administration every other day for a total of 12 times: the AD group with 30 μL saline, OT-Lipo treatment group with 30 μL OT-Lipo containing 2.7 mg/kg OT, and OT-Lipo@M treatment group with 30 μL OT-Lipo@M containing 2.7 mg/kg OT. The intranasal administration method used in this work was modified based on previously published methods [32,33]. Briefly, the mice were lightly anesthetized with isoflurane and manually restrained in the supine position. To avoid respiratory distress and swallowing, the total 30 μL of liquid was divided into 5 to 6 drops and dropped alternately in each nostril using a micropipette (Eppendorf P-100), with an interval of 1–2 min for complete inhalation.

2.14. Open field test

Open field test procedure was adopted from previously described methods [34]. Mice were placed into the center of the apparatus and locomotor behavior such as total moving distance, mean speed and zone crossing number was automatically analyzed using Smart v3.0 video tracking software (RWD Life Science Co. Ltd, China). The apparatus was cleaned with 70% ethanol between two mice and wiped out with clean paper towels.

2.15. Y-maze test

Spatial reference memory was assessed by novel arm recognition test [35]. Briefly, three arms are designated as start arm, other arm and novel arm, and the procedure included training trial and test trial. During training trial, novel arm was closed off and mice were placed into start arm and allowed to explore the maze for 15 min. After a 1-h interval, novel arm was opened for test trial, and mice were re-placed in start arm to freely explore all three arms for 5 min. The percentage of each arm to all arms in terms of distance traveled, time spent, and number of entries were analyzed using Smart v3.0 Video Tracking Software (RWD Life Science Co. Ltd, China). Spatial working memory was assessed by allowing mice to explore all opened three arms freely for 8 min. The number of arm entries were recorded and the percentage of the alternation behavior were calculated.

2.16. Two-day water maze

A two-day water maze test protocol was used to assess spatial learning and memory as previously reported [36]. A platform (8 cm in diameter) located in the center of the northwest quadrant. On day 1, the platform was placed 1 cm above the water surface, and the mice were placed in the pool facing the wall alternately from due east and due south of the pool farthest from the platform to explore for 180 s, a total of 4 times (4 trials), with 1-h intervals between each trial. On day 2, the platform was placed 1 cm below the water level, and the mice were placed in the pool as described above to explore for 180 s, a total of 3 times (3 trials), with 1-h intervals between each trial. The swimming trajectories of mice were recorded using Smart v3.0 video tracking

software (RWD Life Science Co. Ltd, China) and their escape latency, i.e. the time to find the platform, was measured.

2.17. In vivo 9.4T brain MRI

MRI acquisitions were performed on a 9.4T MRI scanner (Bruker BioSpec 94/30 USR, Germany). Mice were anesthetized with isoflurane (5% for induction, 1–2% for maintenance). For brain structural MRI, the 2D T2-weighted TurboRARE sequence was first scanned according to the following parameters: repetition time (TR) = 3205 ms, echo time (TE) = 33 ms, field of view (FOV) = 15 mm × 15 mm, number of slices = 20, slice thickness = 1 mm. Then, the 3D T2-weighted TurboRARE sequence was scanned according to the following parameters: TR = 1800 ms, TE = 37 ms, RARE factor = 12, FOV = 18 mm × 18 mm × 9 mm, number of slices = 60, slice thickness = 0.15 mm. For hippocampus volume analysis, the acquired MR DICOM files were converted to NIFTI format using dcmniix, with augmentation of the voxel size 3 times using DPABI [37]. Automatic segmentation of hippocampus was performed based on Turone Mouse Brain Atlas and Template (TMBTA) using SPM12 software [38]. TMBTA defined the mouse hippocampus into 7 subregions, including hippocampal formation, CA1 field, CA2 field, CA3 field, molecular layer of Dentate gyrus (DG), polymorph layer of DG, and granule cell layer of DG. The volumes of the relevant layers of DG were summed to measure total DG, and the volumes of all subregions were summed to measure total hippocampus. To exclude differences in intracranial size, total intracranial volume (TIV) was calculated as the concomitant variable for normalization of hippocampal volume. For brain T2 map imaging, the multiple gradient-echo sequence was scanned according to the following parameters: TR = 850 ms, TE = 4 ms, flip angle = 25°, FOV = 18 mm × 18 mm, number of slices = 18, slice thickness = 0.141 mm. For analysis, the hippocampus was manually defined as a region of interest (ROI) in MR imaging slices of each mouse, taking care to avoid erroneous inclusion of the CSF signals. The hippocampal T2 values of the different slices of each mouse were averaged and used as the final measurement [39].

2.18. Hippocampal long-term potentiation (LTP) recordings

The mice were sacrificed and brain tissues were rapidly removed and placed at 0 °C into oxygenated artificial cerebrospinal fluid (ASCF) containing 120 mM NaCl, 2.5 mM KCl, 1.25 mM $NaH_2PO_4{\cdot}2H_2O$, 26.2 mM $NaHCO_3$, 1.3 mM $MgSO_4$, 11 mM $C_6H_{12}O_6$ H_2O, and 2.5 mM $CaCl_2$. Then, brain tissues were cut into 400 μm thick brain slices using a vibrating tissue slicer (VF-2000, Compresstome, USA). Brain slices were incubated at 33 °C in oxygenated ACSF for at least 1 h, and then transferred to the MEA (MEA2100-60, Reutlingen, Germany) perfusion chamber. A homemade nylon mesh was placed above the brain slices to ensure a tight fit between the brain slices and the electrode array. The MEA consists of 60 extracellular electrodes with an electrode spacing of 200 μm. Each electrode can be served as both a stimulating electrode and a recording electrode. After recording a 20-min baseline, high-frequency stimulation (HFS, 1 sweep of 100 pulses, 1 s apart) was applied on the electrode located in the SC of the hippocampus to induce the LTP using an external stimulator (STG-1004, Multi-Channel Systems, Germany) [40]. The field excitatory postsynaptic potentials (fEPSPs) in the hippocampal CA1 region were subsequently recorded for 100 min by LTP-Director 1.3.2 and LTP-Analyzer1.3.2. The data were further analyzed using Multi-Channel Systems.

2.19. Western blotting analysis

Proteins were extracted from liposome samples, BV-2 cells, and hippocampal tissues. Protein concentrations in all groups were normalized to be equivalent using a BCA protein detection kit, and equal amounts of protein were resolved by SDS-PAGE and subsequently transferred to polyvinylidene fluoride (PVDF) membranes. After blocking for 1 h at room temperature, the membranes were incubated with the primary antibodies as shown in Table S1 at 4 °C overnight. After washing with Tris-buffered saline with Tween (TBST), the membranes were incubated with secondary antibodies for 1 h at room temperature. After washing with TBST, the protein bands were visualized by the ECL method using ChemiDoc XRS + System (Bio-Rad, USA) and protein expression levels were quantified using ImageJ software.

2.20. Whole-brain TUNEL and immunofluorescence staining

To investigate apoptosis *in vivo*, the brain tissues were removed for terminal deoxynucleotidyl transferase dUTP nick end labeling (TUNEL) assays using an in situ cell death detection kit. For immunofluorescence staining, the paraffin sections were incubated with anti-Aβ (1:100, Abcam) at 4 °C overnight. Then the sections were incubated with the appropriate fluorescent-conjugated secondary antibody (1:2000, Zhongshan Jinqiao) at room temperature for 1 h. The images were obtained using Pannoramic digital scanners (3D HISTECH, Hungary).

2.21. Measurement of brain ROS levels

Brain tissue ROS assay was performed based on the oxidation of DCFH-DA (2′,7′-Dichlorodihydrofluorescein diacetate) to DCF (2′,7′-Dichlorofluorescein) according to previous protocol [41]. Briefly, brain tissues in each group were immediately collected after treatments and homogenized in PBS containing PMSF by a bead beater (Precellys Evolution, Bertin Technologies, USA), and the homogenate was centrifuged at 10,000×*g* for 10 min at 4 °C. The supernatant was diluted 1:2 with PBS, and incubated with DCFH-DA (10 μM) at 37 °C in the dark for 20 min. The DCF fluorescence intensity at an emission wavelength of 525 nm excited at 488 nm was then detected using a fluorospectro photometer (F-7000, Hitachi, Japan). The normalized data was expressed as a value of 100%.

2.22. In vivo biosafety

After the treatment, blood samples were collected from the mice in each group to detect routine blood and serum biochemistry including white blood cells (WBC), red blood cells (RBC), hemoglobin (HGB), platelet (PLT), alanine aminotransferase (ALT), aspartate transaminase (AST), blood urea nitrogen (BUN), albumin (ALB), creatinine (CR), and total bilirubin (TBIL). The nasal septum and major organs (heart, liver, spleen, lung, and kidney) were collected and fixed with 4% paraformaldehyde for 24 h, and paraffin-embedded tissue sections were prepared for Hematoxylin/eosin staining and then observed under a Pannoramic digital scanners (3D HISTECH, Hungary).

2.23. Statistical analysis

Statistical analyses were performed using SPSS25 software. All data were normally distributed (Shapiro-Wilk normality test) and expressed as mean ± SD or mean ± SEM. Significant differences were assessed using Student's t-test or one-way analysis of variance (ANOVA) followed by Tukey's post hoc test (equal variances) or Dunnett's T3 post hoc test (unequal variances). Values of $p < 0.05$ were considered as statistically significant ($^*p < 0.05$, $^{**}p < 0.01$, $^{***}p < 0.001$, $^{****}p < 0.0001$).

3. Results and discussion

3.1. Fabrication and characterization of OT-Lipo@M

OT-loaded liposomes (OT-Lipo) were first prepared by the thin film-hydration method, followed by extrusion and centrifugation to optimize size to 100.89 ± 8.33 nm (PDI = 0.059 ± 0.039) (Fig. 1a). Meanwhile, macrophage membranes (MM) extracted from mouse leukaemic monocyte-macrophage cells (RAW 264.7) were extruded to obtain

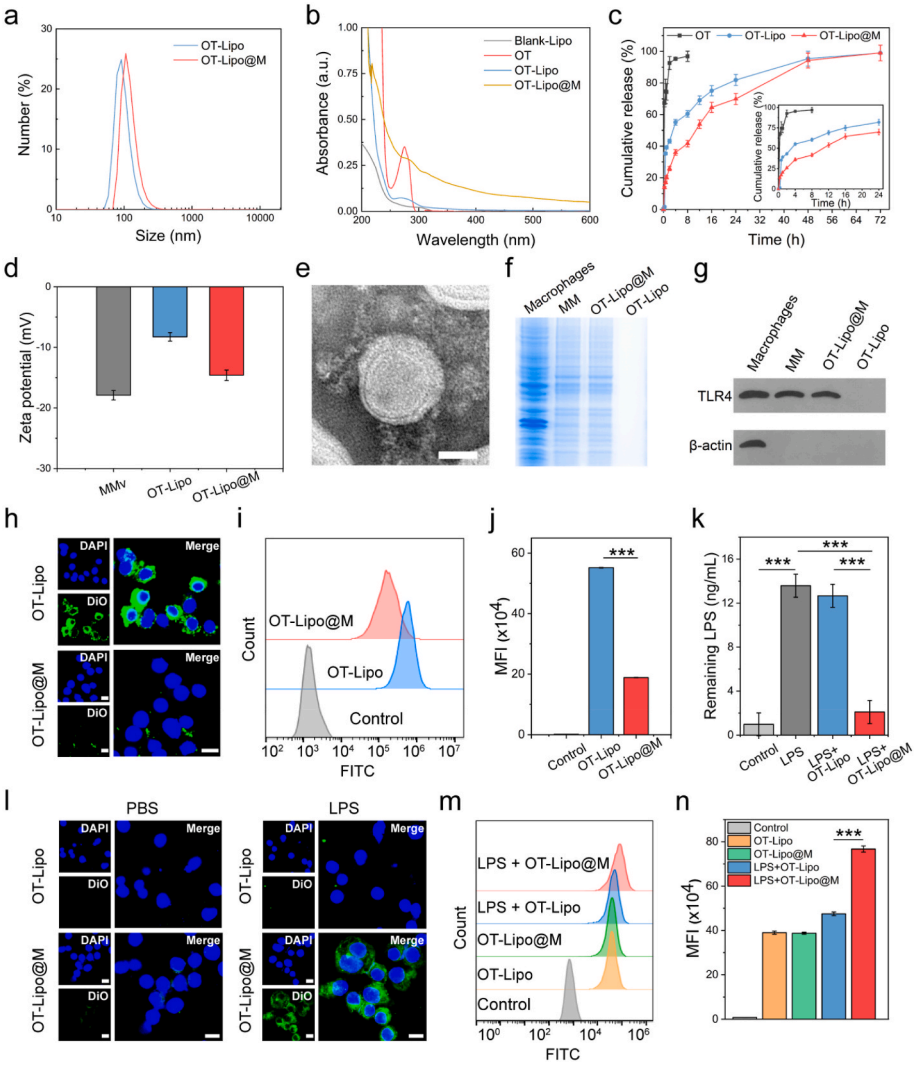

Fig. 1. Fabrication, characterization, and biomimetic properties of OT-Lipo@M. a) DLS sizes. b) UV–vis absorption spectra. c) *In vitro* release profiles of OT from free OT, OT-Lipo and OT-Lipo@M in PBS (pH = 7.4) over time ($n = 3$). d) Zeta potentials ($n = 3$). e) TEM image of OT-Lipo@M. Scale bar: 50 nm. f) Protein profiles determined by Coomassie blue-stained SDS-PAGE. g) Representative immunoblots of TLR4 levels determined by western blotting. h) CLSM images of RAW 264.7 cells uptake of DiO-labeled OT-Lipo or OT-Lipo@M. Scale bars: 20 μm. i) FCM results for cells in h) and j) the corresponding mean fluorescence intensity (MFI) quantification ($n = 3$). k) Remaining LPS content after incubation with OT-Lipo or OT-Lipo@M determined by ELISA ($n = 5$). l) CLSM images of BV-2 cells stimulated with PBS or LPS and treated with DiO-labeled OT-Lipo or OT-Lipo@M. Scale bars: 20 μm. m) FCM results for cells in l) and n) the corresponding MFI quantification ($n = 3$). Data are presented as mean ± SD. ***$p < 0.001$, one-way ANOVA followed by Tukey's post hoc test in j, k) and Dunnett's post hoc test in n).

homogeneous vesicles. Macrophage membrane vesicles (MMv) and OT-Lipo were then co-extruded to obtain OT-Lipo@M with a uniform particle size of 111.27 ± 9.64 nm (PDI = 0.037 ± 0.027) (Fig. 1a). Both OT-Lipo and OT-Lipo@M exhibited characteristic UV–visible absorption of OT at 275 nm, indicating the successful OT encapsulation (Fig. 1b and Fig. S1). The calculated encapsulation efficiency (EE%) and loading capacity (LC%) of OT in OT-Lipo were 33.9 ± 4.3% and 15.9 ± 2.1%, respectively, while those in OT-Lipo@M were decreased to 32.3 ± 1.1% and 8.7 ± 1.1%, respectively (Fig. S2). Both OT-Lipo@M and OT-Lipo could release OT slowly and almost completely at 72 h, while the release rate of OT-Lipo@M within 24 h was about 10% lower than that of OT-Lipo (Fig. 1c). Moreover, no significant particle size increase or aggregation was observed in various biological media, including PBS, DMEM, and DMEM containing 10% FBS at 4 °C within 7 days (Fig. S3), indicating good colloidal stability of OT-Lipo@M.

Negative surface charge of MMv reduced zeta potential from −9.36 ± 0.69 mV of OT-Lipo to −14.6 ± 0.87 mV of OT-Lipo@M (Fig. 1d), suggesting the successful macrophage membrane coating. As shown in Transmission electron microscope (TEM) images, compared with the naked spherical structure of OT-Lipo (Fig. S4), OT-Lipo@M clearly exhibited a core-shell yolk-like structure with a shell thickness of about 9 nm (Fig. 1e), which was consistent with particle size difference in DLS results (Fig. 1a) and comparable to the average cell membrane thickness of 7.5–10 nm [42]. Coomassie blue-stained sodium dodecyl sulfate polyacrylamide gel electrophoresis (SDS-PAGE) was performed to examine the surface protein profile of OT-Lipo@M, which was found very similar to that of macrophages and MM, whereas no membrane protein was found on OT-Lipo (Fig. 1f). Since TLR4 is a key PRR capable of binding neurotoxins, western blotting was then performed to confirm the presence of TLR4 on OT-Lipo@M. The β-actin signal was detected only in macrophages, but not in MM and OT-Lipo@M, demonstrating the high purity of isolated membranes (Fig. 1g). A distinct band corresponding to TLR4 was observed on OT-Lipo@M as well as on macrophages and MM, but not on OT-Lipo (Fig. 1g), demonstrating that intact macrophage membranes were successfully coated on OT-Lipo@M without impaired functional proteins. Moreover, dual-color fluorescein-labeled OT-Lipo@M was prepared by co-extrusion of DiL-labeled OT-Lipo and DiO-labeled MM and incubated with BV-2 cells. CLSM images showed a strong co-localized yellow fluorescence signals in the cytoplasm (Fig. S4), proving the successful and stable combination of OT-Lipo and MM, laying the foundation for OT-Lipo@M to exert a synergistic therapeutic effect.

3.2. *Diverse macrophage-biomimetic properties inherited by OT-Lipo@M*

Next, we verified various biomimetic properties endowed by coating macrophage membranes to OT-Lipo@M through a series of *in vitro* experiments. Firstly, natural membranes can help nanomedicines escape from capture and clearance by mononuclear phagocyte system (MPS), greatly increasing their bioavailability [43]. To assess this

anti-phagocytic effect, cellular endocytosis of OT-Lipo@M and OT-Lipo in RAW 264.7 cells were visualized by labeling with the lipophilic green fluorescence probe DiO under CLSM. Compared with the strikingly high green fluorescence signal in the cytoplasm after OT-Lipo treatment, the intracellular green fluorescence signal was almost imperceptible after OT-Lipo@M treatment (Fig. 1h), revealing the potential of OT-Lipo@M to evade immune surveillance. This result was further confirmed by the significantly weakened fluorescence intensity in OT-Lipo@M-treated cells compared to OT-Lipo-treated cells as shown by flow cytometry (FCM) analysis (Fig. 1i and j).

Secondly, due to the strong affinity of TLR4 for neurotoxins such as LPS, macrophage membrane coating is expected to reduce free LPS content through competitive binding [8,9]. To evaluate this detoxification ability, the amount of remaining LPS after incubation with OT-Lipo@M and OT-Lipo, respectively, was determined by ELISA assay (Fig. S6). The results showed that OT-Lipo@M incubation resulted in a prominent drop in LPS levels, while LPS levels after OT-Lipo incubation were almost as high as untreated free LPS (Fig. 1k), demonstrating the excellent biological neutralization of OT-Lipo@M. Finally, macrophage membrane coating can help nanomedicines target inflammatory sites,

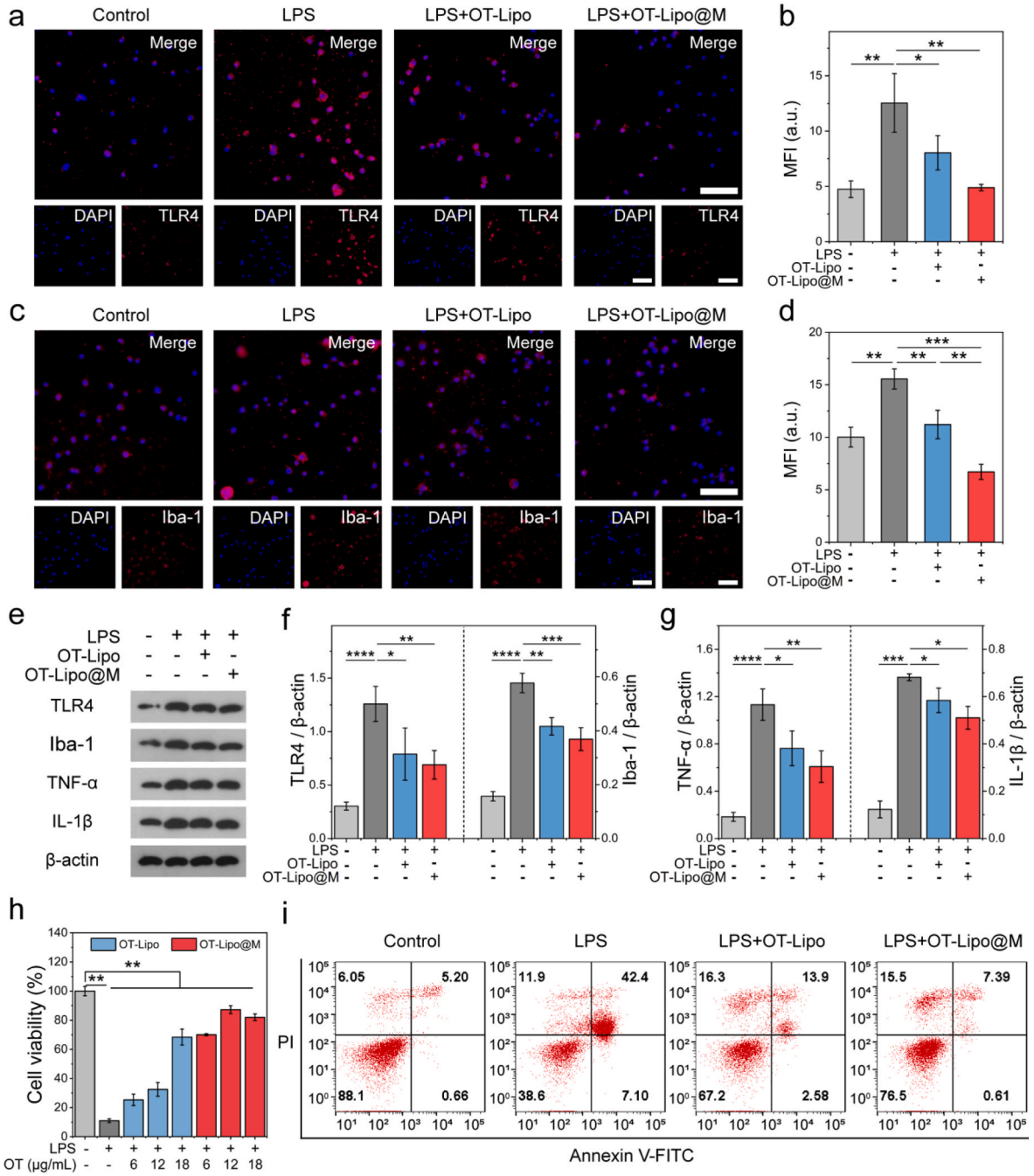

Fig. 2. OT-Lipo@M alleviates TLR4-mediated microglial inflammatory response for neuroprotection. a) Immunofluorescence staining of TLR4 in BV-2 cells and b) the corresponding mean fluorescence intensity (MFI) analysis ($n = 3$). Scale bars: 100 μm. c) Immunofluorescence staining of Iba-1 in BV-2 cells and d) the corresponding MFI analysis ($n = 3$). Scale bars: 100 μm. e) Representative immunoblots and f,g) quantitative analysis for TLR4, Iba-1, TNF-α, and IL-1β in BV-2 cells ($n = 3$). h) Cell viability of HT22 cells after various BV-2 CM treatments determined by CCK-8 assay ($n = 3$). i) FCM analysis of HT22 cell apoptosis after various BV-2 CM treatments. Data are presented as mean ± SD. $^{*}p < 0.05$, $^{**}p < 0.01$, $^{***}p < 0.001$, $^{****}p < 0.0001$, one-way ANOVA followed by Tukey's post hoc test in b, d, f, g) and Dunnett's post hoc test in h).

thereby improving actual efficacy and avoiding side effects [44]. To confirm this inflammation-tropism capability, LPS-stimulated mouse microglia BV-2 cells were used as an *in vitro* inflammatory model to investigate cellular endocytosis of DiO-labeled OT-Lipo@M and OT-Lipo. As expected, OT-Lipo@M exhibited significantly enhanced uptake only in inflamed cells, while OT-Lipo showed equally low uptake under either PBS or LPS stimulation (Fig. 1l–n). These results revealed that, inheriting the advantages of macrophage-derived properties, OT-Lipo@M can serve as a promising nanoantidote with great potential to actively orientate inflammatory lesions and effectively neutralize neurotoxins.

3.3. OT-Lipo@M alleviates TLR4-mediated microglial inflammatory response for neuroprotection

Microglia has been recognized to establish intercellular communication with neurons through their derived mediators to regulate neuronal responses and fate, which play a pivotal role in AD progression. BV-2 and HT22 cells, widely recognized *in vitro* models of mouse microglia and hippocampal neurons, respectively, showed nearly 100% survival after incubation with OT-Lipo or OT-Lipo@M (Fig. S7), suggesting negligible neurotoxicity of this nanoantidote. Consistent with previous reports [45], LPS stimulation had little effect on the viability of BV-2 cells (Fig. S8). However, immunofluorescence imaging revealed that LPS stimulation resulted in a marked increase in TLR4 expression in BV-2 cells (Fig. 2a and b) and aggravated staining of ionized calcium-binding adaptor molecule 1 (Iba-1), a marker of microglial activation (Fig. 2c and d). Encouragingly, OT-Lipo@M treatment exhibited a stronger inhibitory effect than OT-Lipo treatment on LPS-stimulated TLR4 and Iba-1 elevation (Fig. 2a–d). To further investigate the role of different components of OT-Lipo@M, immunofluorescence imaging of TLR4 and Iba-1 was performed after various treatments including Lipo@M treatment. The results revealed that the upregulation of TLR4 and Iba-1 after LPS stimulation was somewhat attenuated after OT-Lipo treatment or Lipo@M treatment, but was significantly downregulated after OT-Lipo@M treatment (Fig. S9). These results suggested that OT release combined with macrophage-biomimetic properties could synergistically inhibit TLR4 expression and its-mediated microglial overactivation.

Western blotting analysis showed that the aberrant upregulation of TLR4 and Iba-1 under LPS stimulation was significantly attenuated after OT-Lipo treatment, which was more pronounced after OT-Lipo@M treatment (Fig. 2e and f). To further assess the resulting inflammatory products, the expression levels of typical pro-inflammatory cytokines such as tumor necrosis factor alpha (TNF-α) and interleukin (IL)-1β in BV-2 cells were analyzed by western blotting, showing that both levels significantly increased by LPS stimulation were more reduced by OT-Lipo@M treatment than OT-Lipo treatment (Fig. 2e,g). The levels of TNF-α and IL-1β in the supernatant of BV-2 cells detected by ELISA assay also showed a similar trend among different treatments (Fig. S10). Then, to investigate the neuroprotective effect benefiting from inflammation remission, conditioned media (CM) from BV-2 cells after various treatments were applied to HT22 cells as previously reported [46]. The viability of HT22 cells cultured in LPS-stimulated BV-2 CM dropped sharply to 10.96%, which was gradually increased by OT-Lipo conditioned treatment in a concentration-dependent manner (Fig. 2h). Impressively, OT-Lipo@M conditioned treatment exhibited very strong protective effect on the survival of HT22 cells, increasing the viability up to 87.22% at 12 μg/mL of OT, much higher than 32.5% raised by OT-Lipo conditioned treatment (Fig. 2h). Subsequently, FCM analysis based on Annexin V-FITC/PI staining showed that OT-Lipo@M conditioned treatment reduced the apoptotic rate of HT22 cells from 49.5% by LPS stimulation to 8.0%, more efficient than 16.48% by OT-Lipo conditioned treatment (Fig. 2i). Taken together, OT-Lipo@M could alleviate TLR4-mediated microglial inflammatory response, thereby suppressing inflammation-induced neuronal apoptosis.

3.4. Brain-targeted and intracerebral inflammation-tropism efficiency of OT-Lipo@M

Overcoming the blood-brain barrier (BBB) is a common challenge for drugs for brain diseases. Although intravenously administered nanocarriers can cross the BBB through transporter modification, low bioavailability and side effects associated with systemic exposure cannot be ignored. Furthermore, such long-term invasive treatment is not advisable for chronic CNS diseases such as AD [47]. Nasal-to-brain delivery has emerged as a compelling noninvasive alternative to directly target the brain by bypassing the BBB through the olfactory bulb and trigeminal nerve pathways [48]. Therefore, intranasal administration of OT-Lipo@M was adopted in this work for *in vivo* AD treatment.

To assess the brain-targeted efficiency, OT-Lipo@M and OT-Lipo labeled with the lipophilic red fluorescence probe DiL were intranasally administered into C57BL/6J mice for *in vivo* fluorescence imaging, respectively. For both DiL-labeled OT-Lipo and OT-Lipo@M, fluorescence signals were observed in living mouse brain at 10 min post administration (Fig. 3a), demonstrating rapid intracerebral transport. Brain fluorescence reached the strongest at 24 h post administration, and then weakened but a little retained at 48 h post administration, during which the accumulation of OT-Lipo@M in the brain was higher than that of OT-Lipo (Fig. 3b and c; Figs. S11–13). As shown by *ex vivo* tissue-based biodistribution, OT-Lipo was abundantly enriched in the liver at 8.5 h post administration and then gradually metabolized, while the hepatic uptake of OT-Lipo@M was consistently low (Fig. 3b,d; Fig. S13), further confirming the anti-phagocytic effect of OT-Lipo@M revealed by *in vitro* results (Fig. 1h–j). Moreover, plasma pharmacokinetics results based on DiL labeling showed that the fluorescence intensity of OT-Lipo in the plasma declined sharply at 4 h post administration, while that of OT-Lipo@M decreased much more slowly, reaching a similar low level at 48 h post administration and almost disappearing at 96 h post administration (Fig. S14). Subsequent fluorescence observation of brain cryosections showed that the amount of DiL-labeled red fluorescence in the hippocampus and cortex was significantly higher after OT-Lipo@M administration than after OT-Lipo administration (Fig. 3e). These results suggested that intranasally administered OT-Lipo@M could efficiently enter the brain and reach AD characteristic lesions assisted by macrophage-biomimetic immune surveillance escape and relatively long blood circulation.

It has been reported that stereotactic injection of LPS into the brain can induce microglial activation, the release of a variety of pro-inflammatory mediators, and cognition dysfunction, which has become the common approach for modeling neuroinflammation *in vivo* [49,50]. To further verify the inflammation-tropism efficiency in AD characteristic lesions, an *in vivo* local inflammation model was established by stereotactic injection of LPS into the right hippocampus of C57BL/6J mice, followed by intranasal administration of DiL-labeled OT-Lipo@M and OT-Lipo, respectively (Fig. 3f). Confocal immunofluorescence imaging of brain cryosections revealed significantly enhanced staining of microglial activation biomarkers, Iba-1 and cluster of differentiation 68 (CD68), in the right hippocampus and cortex of LPS-injected mice compared to sham-operated mice (Fig. 3g,i; Fig. S15), indicating LPS-induced local inflammatory episodes. Considerably strong DiL-labeled red fluorescence signals were found in the right hippocampus and cortex of LPS-injected mice after OT-Lipo@M administration, compared with weak DiL-labeled red fluorescence signals in local inflammatory sites in mouse brain after OT-Lipo administration (Fig. 3g,i; Fig. S16). More importantly, OT-Lipo@M exhibited more pronounced colocalization of DiL-labeled red fluorescence with Iba-1 or CD68 staining than OT-Lipo (Fig. 3h,j). These results strongly supported the enhanced endocytosis of OT-Lipo@M in inflamed BV-2 cells (Fig. 1l–n), confirming that OT-Lipo@M inherited the ability of macrophages to be efficiently recruited to inflammation sites *in vivo*, contributing to improve subsequent therapeutic efficacy.

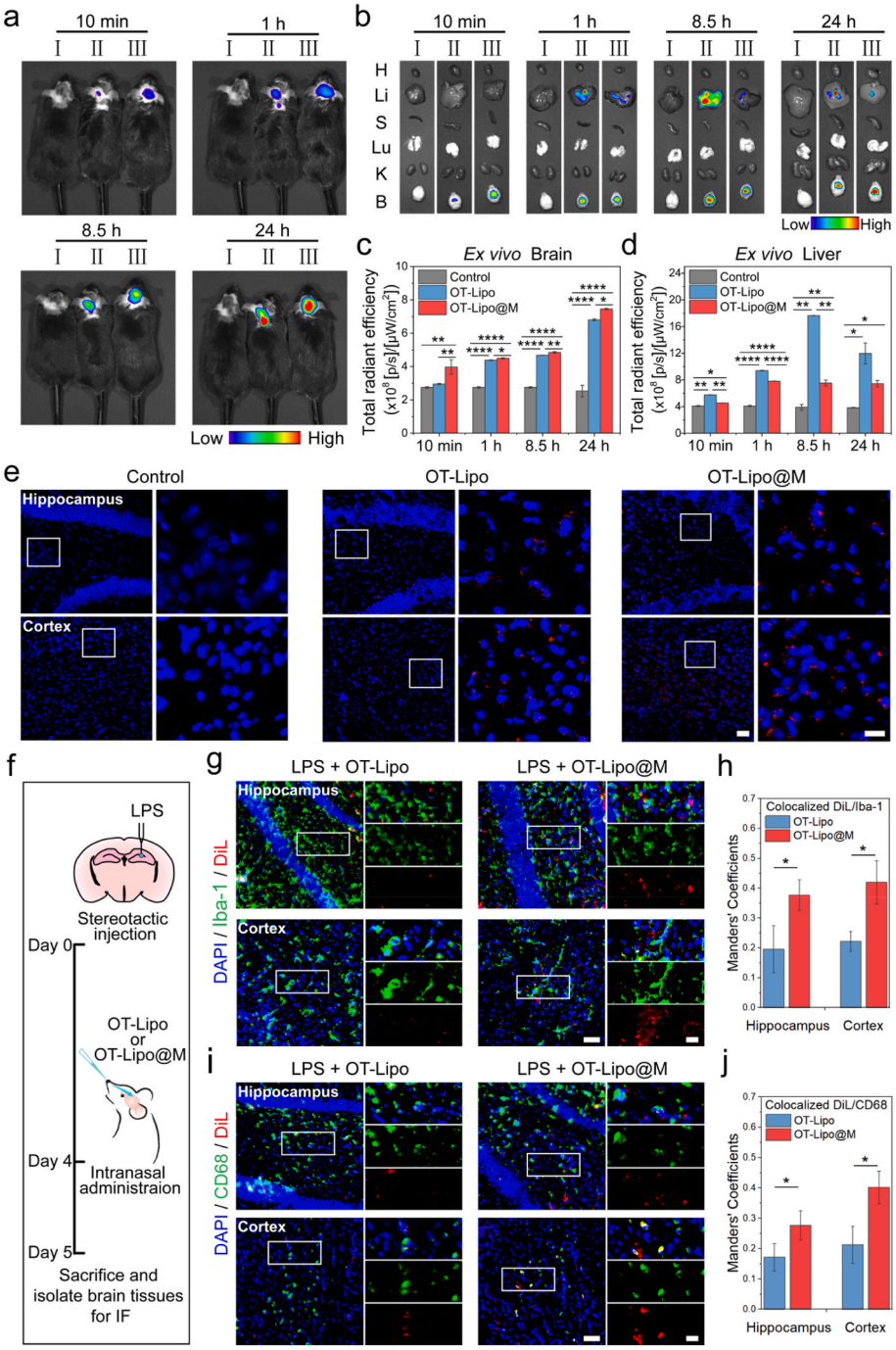

Fig. 3. Brain-targeted and intracerebral inflammation-tropism efficiency of OT-Lipo@M. a) *In vivo* fluorescence images of C57BL/6J mice administered with DiL-labeled OT-Lipo or OT-Lipo@M at indicated time points. b) *Ex vivo* fluorescence images of isolated brain tissues and major organs (H: heart, Li: liver, S: spleen, Lu: lung, K: kidney and B: brain) at indicated time points. Group number: I: Control; II: OT-Lipo; III: OT-Lipo@M. c,d) Quantitative *ex vivo* fluorescence analysis of c) brain and d) liver ($n = 3$). e) Fluorescence images of the hippocampus and cortex in brain cryosections of C57BL/6J mice after DiL-labeled OT-Lipo or OT-Lipo@M administration. Red: DiL labeling; Blue: DAPI. Scale bars: 50 μm for overview images, 20 μm for magnified images. f) Schematic schedule of inflammation-tropism evaluation experiment. g,i) Confocal immunofluorescence images of g) Iba-1 and i) CD68 staining in the hippocampus and cortex in brain cryosections of LPS-injected mice after DiL-labeled OT-Lipo or OT-Lipo@M administration. Scale bars: 50 μm for overview images, 20 μm for magnified images. h,j) Quantitative analysis of DiL-labeled red fluorescence colocalized with h) Iba-1 and j) CD68 staining ($n = 3$). Data are presented as mean ± SD. $^*p < 0.05$, $^{**}p < 0.01$, $^{****}p < 0.0001$, one-way ANOVA followed by Tukey's post hoc test in c,d) and Student's *t*-test in h,j).

3.5. OT-Lipo@M treatment ameliorates cognitive deficits in AD mice

Encouraged by the satisfactory *in vitro* efficacy and intracerebral inflammation-tropism efficiency, we further investigated whether OT-Lipo@M could achieve effective treatment in AD mice. As a widely recognized AD animal model, APP/PS1 mice already exhibit many obvious progressive AD pathological features at 24 weeks of age, such as neuroinflammation, Aβ deposition, synaptic plasticity impairment, and cognitive dysfunction [51,52]. Therefore, 24-week-old APP/PS1 mice were selected in this work and intranasally administered with OT-Lipo or OT-Lipo@M every other day for a total of 12 times, followed by a series of assessment procedures that began with various behavioral paradigms including open field, Y-maze, and two-day water maze tests to evaluate cognitive function in mice (Fig. 4a). Open field test (OFT) is commonly used to judge the voluntary movement and emotional behavior of mice [53]. The moving trajectories of AD mice were found to be denser than those of WT mice (Fig. 4b), accompanied by significant increases in quantified total moving distance, mean speed, and zone crossing number (Fig. 4c–e), suggesting that AD mice exhibited hyperkinesia as the previously reported [54]. Both OT-Lipo and OT-Lipo@M treatments exhibited significant effects in reducing the above indicators, and the latter improved the motor performance of AD mice to almost the normal level of WT mice.

Y-maze test utilizes rodents' instinct to explore new environments to reflect the spatial discrimination memory in mice [35,55]. Spatial reference memory, contributing to the formation of long-term memory by acquiring general rules through repeated learning, was assessed by examining mice's entry preference for the novel arm that was closed off

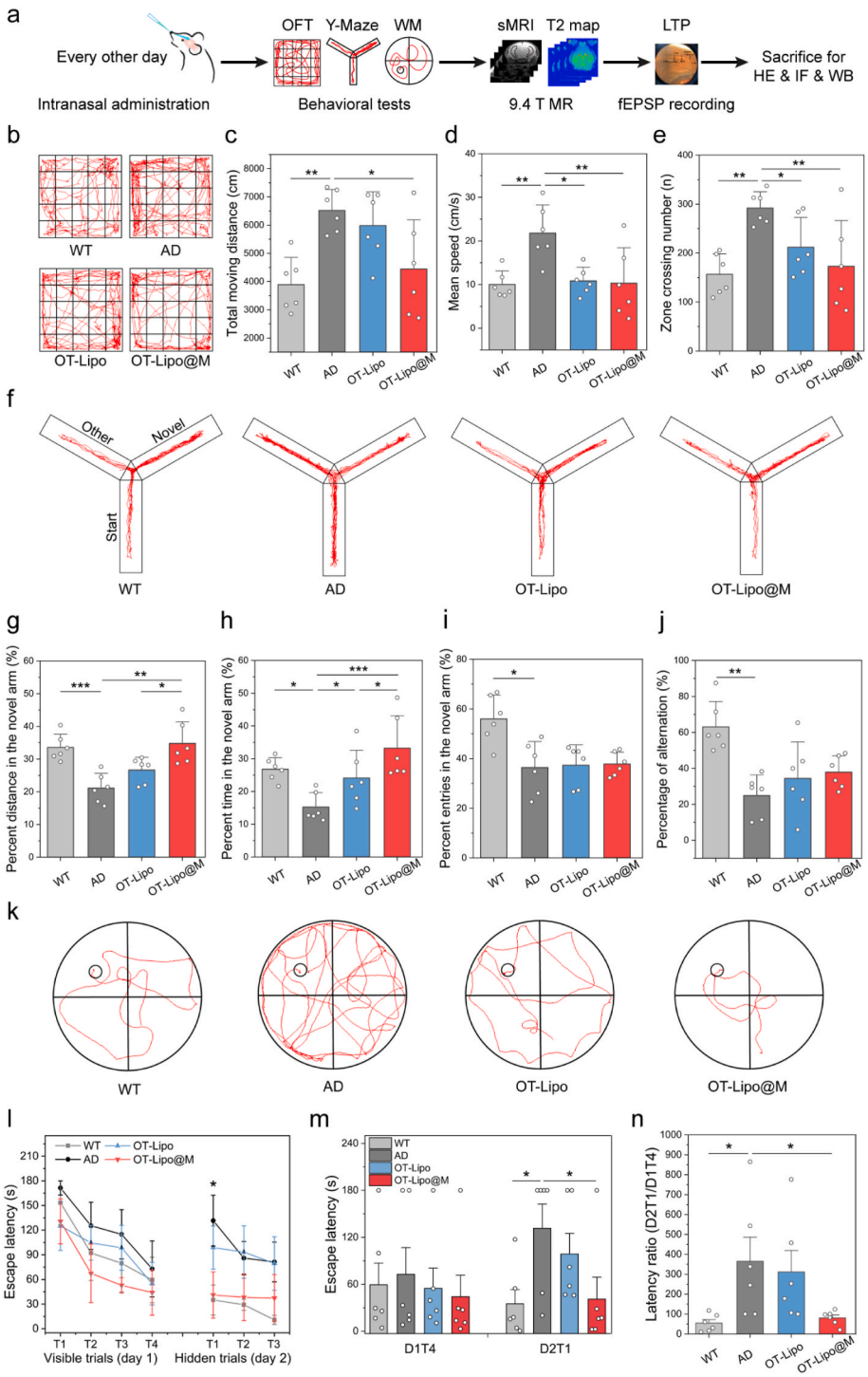

Fig. 4. OT-Lipo@M treatment ameliorates cognitive deficits in AD mice. a) Schematic illustration of *in vivo* treatment and efficacy evaluation. b) Representative moving trajectory, c) total moving distance, d) mean speed, and e) zone crossing number in OFT. f) Representative moving trajectory in Y-maze reference memory test and the percentage of g) distance traveled, h) time spent, and i) number of entries in the novel arm. j) The percentage of spontaneous alternation in Y-maze working memory test. k) Representative swimming paths in the hidden-platform probe phase of two-day water maze test. l) Escape latency recorded for each trial daily. m) Escape latency recorded on day 1 trial 4 (D1T4) and day 2 trial 1 (D2T1). n) Latency ratio by D2T1/D1T4. Data are presented as mean ± SD in c-e), g-j) and mean ± SEM in l-n) ($n = 6$). *$p < 0.05$, **$p < 0.01$, ***$p < 0.001$, one-way ANOVA followed by Tukey's post hoc test.

during the training phase and opened during the test phase [56,57]. The moving traces of WT mice were more concentrated in the novel arm, while AD mice showed no curiosity about the novel arm (Fig. 4f), indicating that APP/PS1 mice had very poor spatial reference memory. Impressively, OT-Lipo@M treatment significantly increased spatial novelty preference in AD mice, showing superior efficacy than OT-Lipo treatment in percentage of distance traveled and time spent in the novel arm (Fig. 4g and h; Fig. S17), without much change in percentage of number of entries (Fig. 4i). There were no significant differences in total distance and mean speed between four groups (Fig. S18), indicating normal motor capacity in all mice. Furthermore, spatial working memory, a form of short-term memory with temporary processing and limited information storage, was assessed by allowing mice to freely explore all three arms [35]. The somewhat reduced number of entries in total arms (Fig. S19) further supported the OFT results (Fig. 4b–e), indicating the inhibitory effect of OT-Lipo@M on AD-induced hyperkinesia. The apparent decline of spontaneous alternation percentage in AD mice was slightly restored by both OT-Lipo and OT-Lipo@M treaments (Fig. 4j).

Two-day water maze test, consisting of four visible-platform training trials on day 1 and three hidden-platform probe trials on day 2, has recently been successfully validated for evaluating spatial learning and

memory impairment in animal models of neurodegenerative diseases [36,58,59]. Compared with traditional Morris water maze (MWM), this paradigm has many advantages as follows [60]. First, visible-platform training reduced the fear and stress caused by the hidden platform in mice, which can avoid desperate floating behavior and reflect more realistic escape behavior. Second, the last training trial on day 1 provided an individual baseline that can improve the sensitivity and accuracy of memory detection on day 2. Finally, the protocol of only two days can greatly save time and labor costs, making it very attractive for behavioral evaluation in aged or CNS disease-affected mice with poor physical and exercise capacity. Therefore, two-day water maze protocol was adopted in this work for evaluating spatial learning and memory in AD mice.

During the visible-platform training phase on day 1, mice in all four groups could find the visible platform, while escape latency was found longer in AD mice than WT mice and obviously shortened in OT-Lipo@M-treated mice (Fig. 4l), indicating that OT-Lipo@M treatment promoted the learning ability of AD mice. During the hidden-platform probe phase on day 2, AD mice spent much more time navigating to the platform than WT mice (Fig. 4k,m), suggesting severely impaired spatial memory in AD mice. Notably, OT-Lipo-treated mice exhibited slightly improved orientation to the platform compared to AD mice,

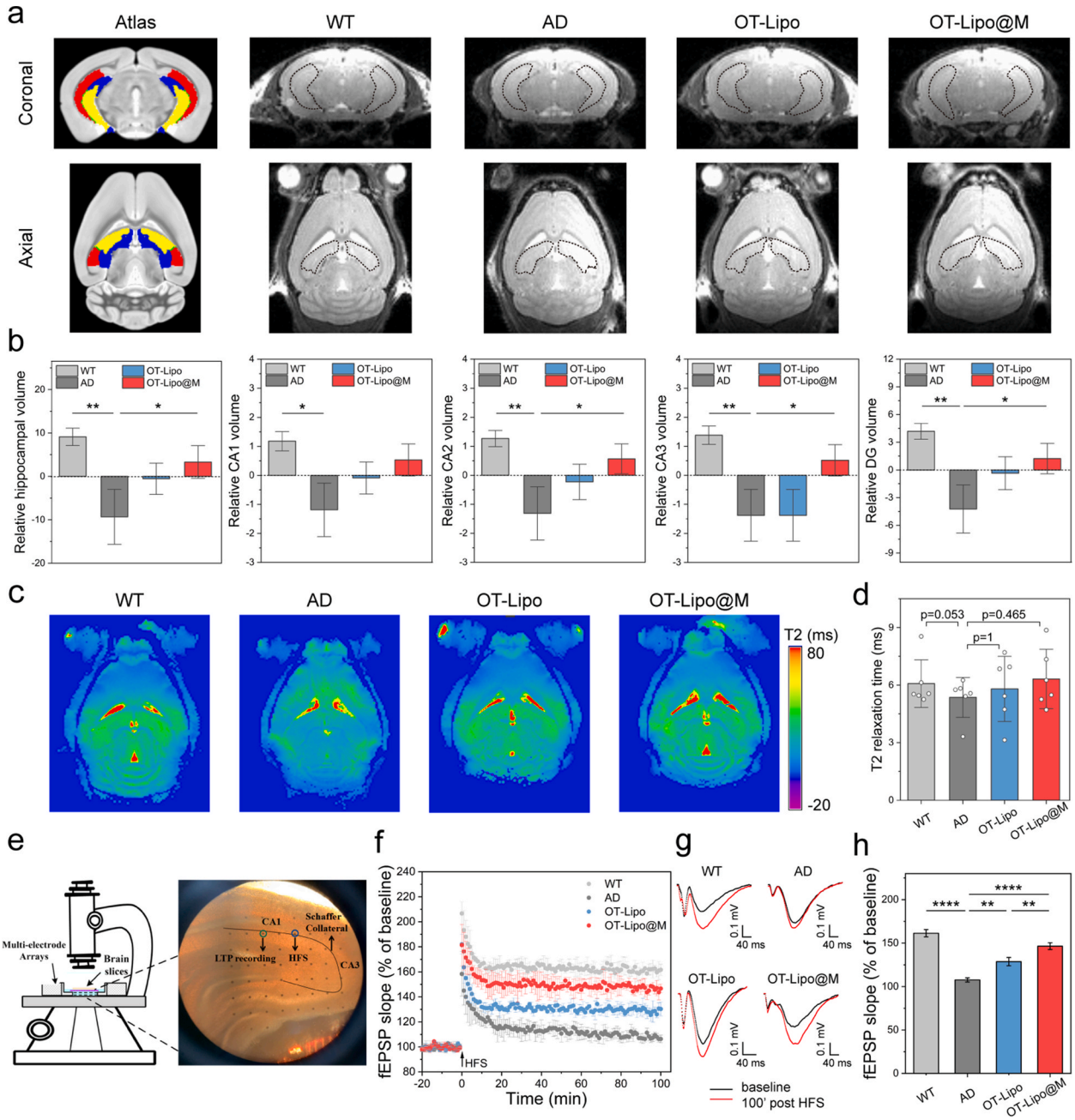

Fig. 5. OT-Lipo@M treatment delays impairments to hippocampal structure and synaptic plasticity. a) Coronal and axial atlas of mouse brain anatomical template annotated with major hippocampal subregions (Red: CA1; Green: CA2; Yellow: CA3; Blue: DG) and representative T2-weighted MRI images of mouse brain with hippocampus location highlighted with black dashed lines. b) Volumetric analysis of the hippocampus and its subregions ($n = 6$). c) Representative T2 map images and d) T2 relaxation time measured in the hippocampus ($n = 6$). e) Schematic of LTP recording at CA3-CA1 synapses in hippocampal slices of mice. f) Normalized fEPSP slopes over time before and after HFS. g) Representative traces of fEPSPs before and at 100 min after HFS. h) Cumulative measurement of mean fEPSP slopes from 91 min to 100 min after HFS (9 slices from 3 mice/group). Data are presented as mean ± SD. *$p < 0.05$, **$p < 0.01$, ****$p < 0.0001$, one-way ANOVA followed by Tukey's post hoc test.

while OT-Lipo@M-treated mice reached the platform almost as quickly as WT mice (Fig. 4k,m). The ratio of escape latency between the first trial on day 2 and the last trial on day 1 (D2T1/D1T4) was further calculated to quantitatively assess the extent of memory retention. The results showed that the D2T1/D1T4 ratio in the AD group was significantly higher than that in the WT group, but was dramatically shortened only by OT-Lipo@M treatment (Fig. 4n). In addition, no significant difference in swimming speed between groups during all trials indicated unimpaired swimming ability (Fig. S20). These findings strongly demonstrated that OT-Lipo@M treatment could remarkedly ameliorate cognitive deficits in AD mice.

3.6. OT-Lipo@M treatment delays impairments to hippocampal structure and synaptic plasticity

Noninvasive advanced magnetic resonance imaging (MRI) technology can provide multi-dimensional structural and functional information of the brain, and its application has high clinical significance for accurate diagnosis and efficacy evaluation of AD [61]. Given that hippocampal atrophy is considered the most important imaging marker of AD, structural MRI (sMRI) was performed immediately following behavioral assessment [62]. Brain sMRI images were acquired using 3D T2-weighted TurboRARE sequence, followed by automatic segmentation of the hippocampus and its subregions based on Turone Mouse Brain Atlas and Template (TMBTA) and corresponding volumetric quantification. The results showed that the marked hippocampal atrophy in AD mice ($p = 0.006$ vs. WT group) was alleviated by both OT-Lipo ($p = 0.157$ vs. AD group) and OT-Lipo@M ($p = 0.047$ vs. AD group) treatments (Fig. 5a and b). The same trend was also observed in all studied subregions, especially in the CA2, CA3 and dentate gyrus (DG) regions, and only OT-Lipo@M treatment significantly reduced volume shrinkage in AD mice (Fig. 5b).

Notably, brain microstructural disruption often precedes volume shrinkage in AD characteristic brain regions such as the hippocampus, which can be assessed by changes in tissue intrinsic MR physical parameters [63]. Among them, T2 relaxation time can reflect the microstructural integrity changes caused by various pathological changes in the brain [64]. Many studies have revealed that AD progression is always accompanied by a decrease in brain T2 values [65,66]. Therefore, T2 mapping MRI was performed using multi-gradient-echo (MGE) sequence to quantitatively detect T2 values in the hippocampus. As shown in axial brain T2 map images, the T2 signal intensity was attenuated in the hippocampus of AD mice compared with WT mice and recovered to some extent after OT-Lipo or OT-Lipo@M treatment (Fig. 5c). Quantitative analysis of T2 values showed that only OT-Lipo@M ($p = 0.465$ vs. AD group) treatment prevented the decline in hippocampal T2 values in AD mice ($p = 0.053$ vs. WT mice) (Fig. 5d). These results suggested that OT-Lipo@M treatment could delay hippocampal atrophy and brain microstructural disruption during AD progression.

Synaptic plasticity is a critical neurobiological basis for learning and memory and plays a key role in information encoding, storage, and persistence [67,68]. Encouraged by OT-Lipo@M improving cognitive function and hippocampal structure in AD mice, we further investigated the impact of OT-Lipo@M treatment on long-term potentiation (LTP) at hippocampal CA3-CA1 synapses (Fig. 5e). Recording of field excitatory postsynaptic potentials (fEPSPs) showed that their slopes decreased sharply in the AD group after application of HFS, which was effectively increased after OT-Lipo treatment and further increased closer to the WT group after OT-Lipo@M treatment (Fig. 5f). Both OT-Lipo and OT-Lipo@M treatments significantly expanded severely compressed fEPSP amplitudes in AD mice at 100 min after HFS (Fig. 5g). Quantitative analysis showed that OT-Lipo@M treatment exhibited more pronounced synaptic potentiation than OT-Lipo treatment (Fig. 5h). These results suggested that OT-Lipo@M treatment could effectively ameliorate the impaired synaptic plasticity in AD mice.

3.7. OT-Lipo@M inhibits TLR4-mediated pro-inflammatory signalling cascade to combat neurodegeneration

To further clarify the underlying molecular mechanisms regulated by OT-Lipo@M, immunofluorescence staining of mouse brain sections was first performed to assess neuronal apoptosis and Aβ deposition distribution. TUNEL (TdT-mediated dUTP nick-end labeling) results showed that green fluorescence-labeled apoptotic cells were increased significantly in the cortex and hippocampus of AD mice, but were barely observed after OT-Lipo@M treatment (Fig. 6a), further confirming the neuroprotective effect of OT-Lipo@M against neuronal apoptosis revealed by *in vitro* results (Fig. 2h and i). Intriguingly, Aβ aggregate staining showed that red fluorescence intensity and distribution accumulated in the cortex and hippocampus of the AD group recovered almost to the same low level as those of the WT group after OT-Lipo@M treatment (Fig. 6b), indicating that OT-Lipo@M exerted a potent inhibitory effect on Aβ deposits in AD mouse brain. In addition, the histological ROS level detection based on DCFH-DA assay showed that OT-Lipo@M treatment greatly inhibited the increase in ROS production in AD mouse brain (Fig. S21), indicating effective alleviation of oxidative stress, further revealing the relief of neurotoxicity by OT-Lipo@M.

Given that Aβ deposits in AD brain can act as a neurotoxin to bind TLR4 and induce pro-inflammatory response, Iba-1 and TLR4 levels in the hippocampus were first examined by western blotting, and their marked decrease suggested that OT-Lipo@M treatment greatly attenuated microglial overactivation and TLR4 upregulation (Fig. 6c and d), consistent with the corresponding cellular results (Fig. 2a–f). Further analysis shows that Myd88 levels were significantly decreased after OT-Lipo@M treatment compared with the AD group (Fig. 6c,e), accompanied by significantly downregulated phosphorylation levels of c-Jun N-terminal protein kinase (JNK) and p38 (Fig. 6g–i), indicating that OT-Lipo@M treatment effectively blocked the recruitment of Myd88 and its induced mitogen-activated protein kinase (MAPK) cascade [69,70]. The resulting inhibition of nuclear factor-κB (NF-κB) expression in the AD group by OT-Lipo@M treatment ultimately effectively reduced the transcriptional upregulation of pro-inflammatory cytokines TNF-α and IL-1β (Fig. 6e and f). These results demonstrated that TLR4/Myd88/MAPK/NF-κB signalling could be inhibited by OT-Lipo@M to ameliorate hippocampal neuroinflammation in AD progression.

Extracellular regulated kinase (ERK)/MAPK signalling plays a vital role in LTP enhancement and memory consolidation [71]. Encouraged by LTP recording results (Fig. 5e–h), ERK phosphorylation was examined and found to be greatly reduced in the AD group, which was significantly reversed by OT-Lipo@M treatment (Fig. 6g,j). The levels of presynaptic protein synapsin 1 (SYN1) and postsynaptic density protein 95 (PSD95) in the hippocampus of OT-Lipo@M-treated mice were also obviously increased compared with AD mice (Fig. 6k,l), further suggesting the protective effect of OT-Lipo@M on synaptic function. Furthermore, the increased levels of proapoptotic proteins caspase-3 and p53 in AD mice were significantly reduced after OT-Lipo@M treatment (Fig. 6k,m), supporting brain TUNEL fluorescence staining results (Fig. 6a). Overall, OT-Lipo treatment showed favorable effects in inhibiting TLR4-mediated pro-inflammatory signalling cascade and rescuing its associated neurodegeneration (Fig. 6n), but OT-Lipo@M showed much stronger efficacy. These findings strongly validated the two-pronged AD therapeutic strategy exerted by OT-Lipo@M through combining macrophage-biomimetic detoxification and neurobiological regulation of OT.

Considering future drug development and possible clinical applications, the biosafety of OT-Lipo@M was preliminarily investigated. Cell viability assays have demonstrated extremely low neurotoxicity of OT-Lipo@M (Fig. S7), most likely attributable to good biocompatibility of human endocrine OT and natural membranes as well as FDA-approved liposome components. After AD mice treated with OT-Lipo or OT-Lipo@M, blood routine parameters (WBC, RBC, HGB and PLT) and

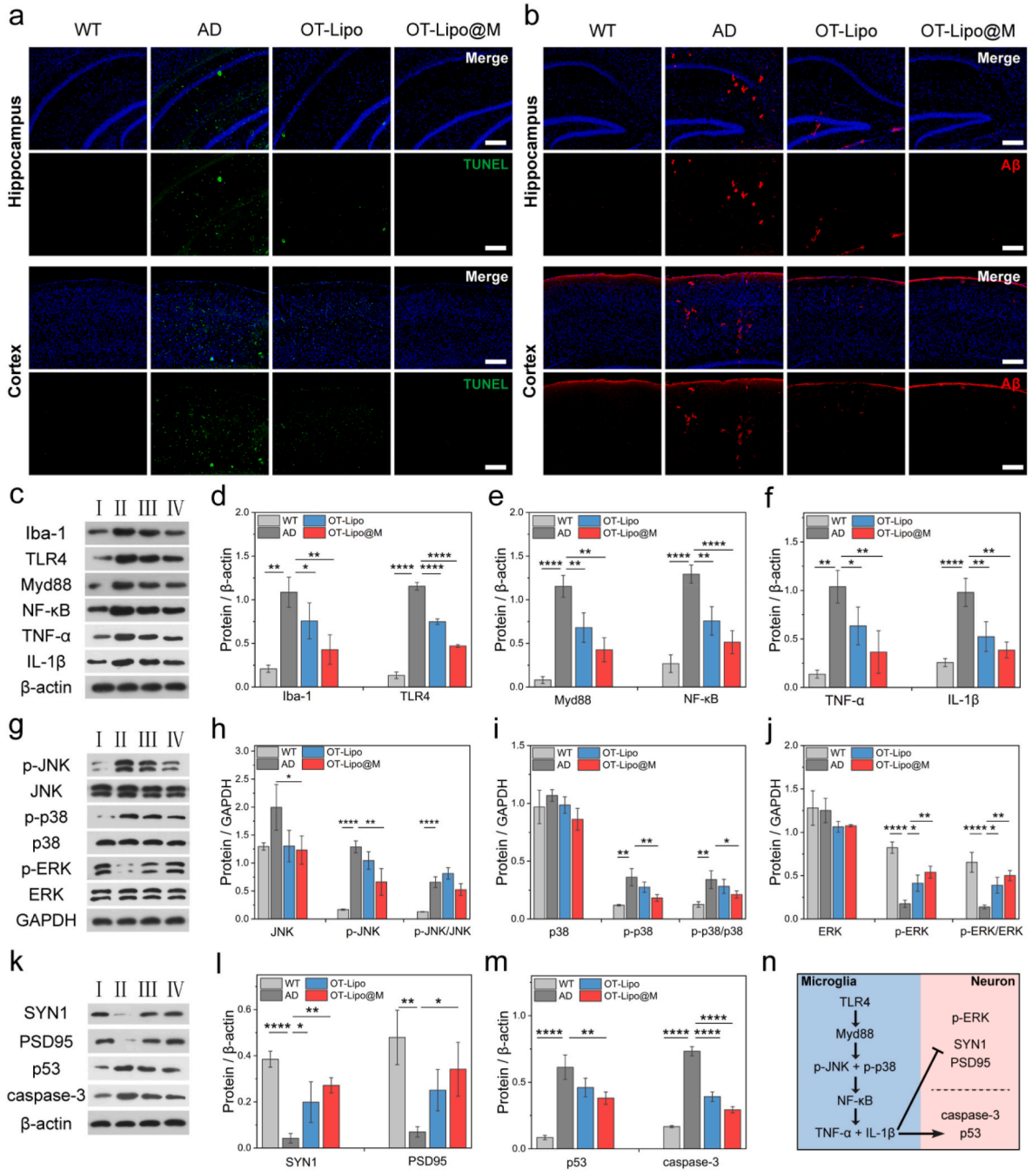

Fig. 6. OT-Lipo@M inhibits TLR4-mediated pro-inflammatory signalling cascade to combat neurodegeneration. a) TUNEL fluorescence images of mouse brain sections. Scale bar: 200 μm. b) Immunofluorescence images of Aβ aggregates of mouse brain sections. Scale bar: 200 μm. c,g,k) Representative immunoblots and quantitative analysis for d) Iba-1 and TLR4, e) Myd88 and NF-κB, f) TNF-α and IL-1β, h) JNK and *p*-JNK, i) p38 and p-p38, j) ERK and *p*-ERK, l) SYN1 and PSD95, and m) p53 and caspase-3 ($n = 3$). Group number: I: WT; II: AD; III: OT-Lipo treatment; IV: OT-Lipo@M treatment. n) Schematic illustration showing the pathological molecular mechanisms regulated by OT-Lipo@M. Data are presented as mean ± SD. $^{*}p < 0.05$, $^{**}p < 0.01$, $^{****}p < 0.0001$, one-way ANOVA followed by Tukey's post hoc test.

serum enzyme levels (ALT, AST, BUN, ALB, CR and TBIL) showed no statistic significant change among four groups, indicating that OT-Lipo@M treatment did not cause any obvious hematological, hepatic, and renal toxicity (Fig. S22). Hematoxylin/eosin staining revealed no notable damage observed in nasal mucosa and main organs (heart, liver, spleen, lung and kidney) (Fig. S23). In addition, although systemic exposure to OT-Lipo@M is very low (Fig. 3b), small amounts of OT released may reach its peripheral target organs, such as the uterus, ovaries, and breasts, so its use should be carefully considered during pregnancy and lactation.

4. Conclusion

In summary, a highly potent and versatile nanoantidote OT-Lipo@M based on macrophage membrane engineering was successfully developed to inhibit neurotoxin-induced immune recognition and pro-inflammatory response for neuroinflammation-targeted therapy in AD. By virtue of the inherent anti-phagocytic and inflammation-tropism properties of coating macrophage membranes, OT-Lipo@M can actively target the neuroinflammatory sites in AD characteristic brain regions. Afterwards, coating macrophage membranes can neutralize

neurotoxins, while OT is released to inhibit immune recognition of neurotoxins by microglia and TLR4-mediated pro-inflammatory signalling cascade, synergistically suppressing inflammation response. Benefiting from significantly relieved chronic neuroinflammation by this therapeutic strategy of OT-Lipo@M, neurodegenerative features including hippocampal atrophy and microstructural disruption, neuronal apoptosis, and impaired synaptic plasticity were all rescued, ultimately promoting the recovery of cognitive function in AD mice. This work highlights the potential of biomimetic nanoantidotes to comprehensively inhibit the onset of microglia-mediated neuroinflammation for AD therapy by neutralizing neurotoxins and suppressing immune recognition. Encouraged by our results, OT-Lipo@M is expected to nip the neuroinflammation-derived AD pathology in the bud and contribute to the early prevention of AD. Moreover, many PRRs other than TLR4 will also serve as blocking targets for microglia to recognize neurotoxins, and thus the loaded drugs will be variable accordingly. Meanwhile, different polarization types of membrane-derived macrophages accompanied by changes in PRR expression deserve further attention in the design of future biomimetic nanosystems.

Data Availability Statement

The data that support the findings of this study are available from the last corresponding author upon reasonable request.

Ethics approval and consent to participate

All animal experiments were performed in accordance with the guidelines approved by the Animal Care and Use Committee of the Institute of Radiation Medicine, Chinese Academy of Medical Sciences (SYXK2019-0002).

CRediT authorship contribution statement

Meng Cheng: Conceptualization, Data curation, Investigation, Formal analysis, Methodology, Writing – original draft. **Caihua Ye:** Investigation, Methodology, Data curation, Formal analysis. **Chunxiao Tian:** Investigation, Data curation, Formal analysis, Methodology. **Dongju Zhao:** Data curation, Formal analysis, Methodology. **Haonan Li:** Data curation, Formal analysis. **Zuhao Sun:** Data curation, Formal analysis, Methodology. **Yuyang Miao:** Data curation, Formal analysis. **Qiang Zhang:** Resources, Data curation, Supervision. **Junping Wang:** Resources, Funding acquisition, Formal analysis, Supervision, Writing – review & editing. **Yan Dou:** Conceptualization, Resources, Data curation, Formal analysis, Supervision, Investigation, Methodology, Project administration, Writing – review & editing.

Declaration of competing interest

The authors declare that they have no known competing financial interests or personal relationships that could have appeared to influence the work reported in this paper.

Acknowledgments

This research was financially supported by the National Natural Science Foundation of China (Grant No. 81871431, 82171905 and 81801828), the Tianjin Natural Science Foundation (Grant No. 21JCQNJC01570 and 22JCYBJC01340), Tianjin Key Medical Discipline (Specialty) Construction Project (TJYXZDXK-001A), Tianjin Municipal Education Research Project (20140115) and Fund for Distinguished Young Scholars of Tianjin Medical University General Hospital (22ZYYJQ03).

Appendix A. Supplementary data

Supplementary data to this article can be found online at https://doi.org/10.1016/j.bioactmat.2023.03.004.

References

[1] F. Leng, P. Edison, Neuroinflammation and microglial activation in Alzheimer disease: where do we go from here? Nat. Rev. Neurol. 17 (2021) 157–172, https://doi.org/10.1038/s41582-020-00435-y.
[2] R.M. Ransohoff, How neuroinflammation contributes to neurodegeneration, Science 353 (2016) 777–783, https://doi.org/10.1126/science.aag2590.
[3] B.T. Casali, E.G. Reed-Geaghan, Microglial function and regulation during development, homeostasis and Alzheimer's disease, Cells 10 (2021) 957, https://doi.org/10.3390/cells10040957.
[4] R.M. McManus, The role of immunity in Alzheimer's disease, Adv Biol (Weinh) 6 (2022), e2101166, https://doi.org/10.1002/adbi.202101166.
[5] G. Piccioni, D. Mango, A. Saidi, M. Corbo, R. Nistico, Targeting microglia-synapse interactions in Alzheimer's disease, Int. J. Mol. Sci. 22 (2021) 2342, https://doi.org/10.3390/ijms22052342.
[6] S. Wang, D. Wang, Y. Duan, Z. Zhou, W. Gao, L. Zhang, Cellular nanosponges for biological neutralization, Adv. Mater. 34 (2022), e2107719, https://doi.org/10.1002/adma.202107719.
[7] M. Liu, H. Lutz, D. Zhu, K. Huang, Z. Li, P.C. Dinh, J. Gao, Y. Zhang, K. Cheng, Bispecific antibody inhalation therapy for redirecting stem cells from the lungs to repair heart injury, Adv. Sci. 8 (2020), 2002127, https://doi.org/10.1002/advs.202002127.
[8] S. Thamphiwatana, P. Angsantikul, T. Escajadillo, Q. Zhang, J. Olson, B.T. Luk, S. Zhang, R.H. Fang, W. Gao, V. Nizet, L. Zhang, Macrophage-like nanoparticles concurrently absorbing endotoxins and proinflammatory cytokines for sepsis management, Proc. Natl. Acad. Sci. U. S. A. 114 (2017) 11488–11493, https://doi.org/10.1073/pnas.1714267114.
[9] Z. Ou, H. Zhong, L. Zhang, M. Deng, W. Zhang, J. Wang, H. Feng, J. Gong, C. Miao, Z. Yi, Macrophage membrane-coated nanoparticles alleviate hepatic ischemia-reperfusion injury caused by orthotopic liver transplantation by neutralizing endotoxin, Int. J. Nanomed. 15 (2020) 4125–4138, https://doi.org/10.2147/ijn.S253125.
[10] N. Khatoon, Z. Zhang, C. Zhou, M. Chu, Macrophage membrane coated nanoparticles: a biomimetic approach for enhanced and targeted delivery, Biomater. Sci. 10 (2022) 1193–1208, https://doi.org/10.1039/d1bm01664d.
[11] R. Zhang, S. Wu, Q. Ding, Q. Fan, Y. Dai, S. Guo, Y. Ye, C. Li, M. Zhou, Recent advances in cell membrane-camouflaged nanoparticles for inflammation therapy, Drug Deliv. 28 (2021) 1109–1119, https://doi.org/10.1080/10717544.2021.1934188.
[12] T. Liang, R. Zhang, X. Liu, Q. Ding, S. Wu, C. Li, Y. Lin, Y. Ye, Z. Zhong, M. Zhou, Recent advances in macrophage-mediated drug delivery systems, Int. J. Nanomed. 16 (2021) 2703–2714, https://doi.org/10.2147/ijn.S298159.
[13] C. Gao, Q. Huang, C. Liu, C.H.T. Kwong, L. Yue, J.B. Wan, S.M.Y. Lee, R. Wang, Treatment of atherosclerosis by macrophage-biomimetic nanoparticles via targeted pharmacotherapy and sequestration of proinflammatory cytokines, Nat. Commun. 11 (2020) 2622, https://doi.org/10.1038/s41467-020-16439-7.
[14] C. Li, Z. Zhao, Y. Luo, T. Ning, P. Liu, Q. Chen, Y. Chu, Q. Guo, Y. Zhang, W. Zhou, H. Chen, Z. Zhou, Y. Wang, B. Su, H. You, T. Zhang, X. Li, H. Song, C. Li, T. Sun, C. Jiang, Macrophage-disguised manganese dioxide nanoparticles for neuroprotection by reducing oxidative stress and modulating inflammatory microenvironment in acute ischemic stroke, Adv. Sci. 8 (2021), e2101526, https://doi.org/10.1002/advs.202101526.
[15] Y. Gao, J. Zhang, S. Li, Y. Zhang, Y. Zhao, C. Chang, Y. Qiu, G. Yang, Cattle encephalon glycoside and ignotin protects neurons against microglia-induced neuroinflammation via elevating BDNF expression and inhibiting TLR4/NF-κB pathway, Neurochem. Res. 46 (2021) 326–336, https://doi.org/10.1007/s11064-020-03168-y.
[16] M. Calvo-Rodriguez, C. García-Rodríguez, C. Villalobos, L. Núñez, Role of toll like receptor 4 in Alzheimer's disease, Front. Immunol. 11 (2020) 1588, https://doi.org/10.3389/fimmu.2020.01588.
[17] C.E. Keogh, K.M. Rude, M.G. Gareau, Role of pattern recognition receptors and the microbiota in neurological disorders, J. Physiol. 599 (2021) 1379–1389, https://doi.org/10.1113/JP279771.
[18] Y.N. Paudel, E. Angelopoulou, C. Piperi, I. Othman, K. Aamir, M.F. Shaikh, Impact of HMGB1, RAGE, and TLR4 in Alzheimer's disease (AD): from risk factors to therapeutic targeting, Cells 9 (2020) 383, https://doi.org/10.3390/cells9020383.
[19] Q. Li, Y. Wu, J. Chen, A. Xuan, X. Wang, Microglia and immunotherapy in Alzheimer's disease, Acta Neurol. Scand. 145 (2022) 273–278, https://doi.org/10.1111/ane.13551.
[20] T. Inoue, H. Yamakage, M. Tanaka, T. Kusakabe, A. Shimatsu, N. Satoh-Asahara, Oxytocin suppresses inflammatory responses induced by lipopolysaccharide through inhibition of the eIF-2-ATF4 pathway in mouse microglia, Cells 8 (2019) 527, https://doi.org/10.3390/cells8060527.
[21] C. Ye, M. Cheng, L. Ma, T. Zhang, Z. Sun, C. Yu, J. Wang, Y. Dou, Oxytocin nanogels inhibit innate inflammatory response for early intervention in Alzheimer's disease, ACS Appl. Mater. Interfaces 14 (2022) 21822–21835, https://doi.org/10.1021/acsami.2c00007.
[22] X. Mou, J. Fang, A. Yang, G. Du, Oxytocin ameliorates bone cancer pain by suppressing toll-like receptor 4 and proinflammatory cytokines in rat spinal cord,

J. Neurogenet. 34 (2020) 216–222, https://doi.org/10.1080/01677063.2019.1711077.
[23] S. Xu, B. Qin, A. Shi, J. Zhao, X. Guo, L. Dong, Oxytocin inhibited stress induced visceral hypersensitivity, enteric glial cells activation, and release of proinflammatory cytokines in maternal separated rats, Eur. J. Pharmacol. 818 (2018) 578–584, https://doi.org/10.1016/j.ejphar.2017.11.018.
[24] X. Yang, X. An, C. Wang, F. Gao, Y. Lin, W. Chen, Q. Deng, D. Xu, S. Li, P. Zhang, B. Sun, Y. Hou, J. Wu, Protective effect of oxytocin on ventilator-induced lung injury through NLRP3-mediated pathways, Front. Pharmacol. 12 (2021), 722907, https://doi.org/10.3389/fphar.2021.722907.
[25] C. Gong, X. Yu, B. You, Y. Wu, R. Wang, L. Han, Y. Wang, S. Gao, Y. Yuan, Macrophage-cancer hybrid membrane-coated nanoparticles for targeting lung metastasis in breast cancer therapy, J. Nanobiotechnol. 18 (2020) 92, https://doi.org/10.1186/s12951-020-00649-8.
[26] d.M. Mbc, D. R, B. v.E, L. G, d.M. Bs, V. M, S. R, K. Rj, Ultrasound-sensitive liposomes for triggered macromolecular drug delivery: formulation and in vitro characterization, Front. Pharmacol. 10 (2019) 1463, https://doi.org/10.3389/fphar.2019.01463.
[27] W. R, S. Y, H. W, C. Y, L. E, S. X, Pulmonary surfactants affinity Pluronic-hybridized liposomes enhance the treatment of drug-resistant lung cancer, Int. J. Pharm. 607 (2021), 120973, https://doi.org/10.1016/j.ijpharm.2021.120973.
[28] H. Cao, Z. Dan, X. He, Z. Zhang, H. Yu, Q. Yin, Y. Li, Liposomes coated with isolated macrophage membrane can target lung metastasis of breast cancer, ACS Nano 10 (2016) 7738–7748, https://doi.org/10.1021/acsnano.6b03148.
[29] H.H. Wu, X.C. Jiang, Y.S. Li, Y. Zhou, T.Y. Zhang, P. Zhi, J.Q. Gao, Engineering stem cell derived biomimetic vesicles for versatility and effective targeted delivery, Adv. Funct. Mater. 30 (2020), https://doi.org/10.1002/adfm.202006169.
[30] J. Nai, J. Zhang, J. Li, H. Li, Y. Yang, M. Yang, Y. Wang, W. Gong, Z. Li, L. Li, C. Gao, Macrophage membrane- and cRGD-functionalized thermosensitive liposomes combined with CPP to realize precise siRNA delivery into tumor cells, Mol. Ther. Nucleic Acids 27 (2022) 349–362, https://doi.org/10.1016/j.omtn.2021.12.016.
[31] L. Rambousek, T. Gschwind, C. Lafourcade, J.C. Paterna, L. Dib, J.M. Fritschy, A. Fontana, Aberrant expression of PAR bZIP transcription factors is associated with epileptogenesis, focus on hepatic leukemia factor, Sci. Rep. 10 (2020) 3760, https://doi.org/10.1038/s41598-020-60638-7.
[32] H.K. Dhaliwal, Y. Fan, J. Kim, M.M. Amiji, Intranasal delivery and transfection of mRNA therapeutics in the brain using cationic liposomes, Mol. Pharm. 17 (2020) 1996–2005, https://doi.org/10.1021/acs.molpharmaceut.0c00170.
[33] Z. Li, Y. Zhang, Y. Zheng, W. Liu, X. Zhang, W. Li, D. Zhang, Q. Cai, S. Wang, X. Meng, G. Huang, Intranasal 15d-PGJ2 ameliorates brain glucose hypometabolism via PPARγ-dependent activation of PGC-1α/GLUT4 signalling in APP/PS1 transgenic mice, Neuropharmacology 196 (2021), 108685, https://doi.org/10.1016/j.neuropharm.2021.108685.
[34] X.J. Cheng, J.X. Gu, Y.P. Pang, J. Liu, T. Xu, X.R. Li, Y.Z. Hua, K.A. Newell, X. F. Huang, Y. Yu, Y. Liu, Tacrine-hydrogen sulfide donor hybrid ameliorates cognitive impairment in the aluminum chloride mouse model of Alzheimer's disease, ACS Chem. Neurosci. 10 (2019) 3500–3509, https://doi.org/10.1021/acschemneuro.9b00120.
[35] A.K. Kraeuter, P.C. Guest, Z. Sarnyai, The Y-maze for assessment of spatial working and reference memory in mice, Methods Mol Biol 1916 (2019) 105–111, https://doi.org/10.1007/978-1-4939-8994-2_10.
[36] Y. Liu, A. Cheng, Y.J. Li, Y. Yang, Y. Kishimoto, S. Zhang, Y. Wang, R. Wan, S. M. Raefsky, D. Lu, T. Saito, T. Saido, J. Zhu, L.J. Wu, M.P. Mattson, SIRT3 mediates hippocampal synaptic adaptations to intermittent fasting and ameliorates deficits in APP mutant mice, Nat. Commun. 10 (2019) 1886, https://doi.org/10.1038/s41467-019-09897-1.
[37] C.G. Yan, X.D. Wang, X.N. Zuo, Zang, Y.F. Dpabi, Data processing & analysis for (Resting-State) brain imaging, Neuroinformatics 14 (2016) 339–351, https://doi.org/10.1007/s12021-016-9299-4.
[38] D.A. Barrière, A. Ella, F. Szeremeta, H. Adriaensen, W. Même, E. Chaillou, M. Migaud, S. Même, F. Lévy, M. Keller, Brain orchestration of pregnancy and maternal behavior in mice: a longitudinal morphometric study, Neuroimage 230 (2021), 117776, https://doi.org/10.1016/j.neuroimage.2021.117776.
[39] A.C. Coan, B. Kubota, F.P. Bergo, B.M. Campos, F. Cendes, 3T MRI quantification of hippocampal volume and signal in mesial temporal lobe epilepsy improves detection of hippocampal sclerosis, AJNR Am J Neuroradiol 35 (2014) 77–83, https://doi.org/10.3174/ajnr.A3640.
[40] Y. Zheng, C. Tian, L. Dong, L. Tian, R.A. Glabonjat, C. Xiong, Effect of arsenic-containing hydrocarbon on the long-term potentiation at Schaffer Collateral-CA1 synapses from infantile male rat, Neurotoxicology 84 (2021) 198–207, https://doi.org/10.1016/j.neuro.2021.04.002.
[41] T. Ali, T. Kim, S.U. Rehman, M.S. Khan, F.U. Amin, M. Khan, M. Ikram, M.O. Kim, Natural dietary supplementation of anthocyanins via PI3K/Akt/Nrf2/HO-1 pathways mitigate oxidative stress, neurodegeneration, and memory impairment in a mouse model of Alzheimer's disease, Mol. Neurobiol. 55 (2018) 6076–6093, https://doi.org/10.1007/s12035-017-0798-6.
[42] T. Sun, C.H.T. Kwong, C. Gao, J. Wei, L. Yue, J. Zhang, R.D. Ye, R. Wang, Amelioration of ulcerative colitis via inflammatory regulation by macrophage-biomimetic nanomedicine, Theranostics 10 (2020) 10106–10119, https://doi.org/10.7150/thno.48448.
[43] J.O. Martinez, R. Molinaro, K.A. Hartman, C. Boada, R. Sukhovershin, E. De Rosa, D. Kirui, S. Zhang, M. Evangelopoulos, A.M. Carter, J.A. Bibb, J.P. Cooke, E. Tasciotti, Biomimetic nanoparticles with enhanced affinity towards activated endothelium as versatile tools for theranostic drug delivery, Theranostics 8 (2018) 1131–1145, https://doi.org/10.7150/thno.22078.
[44] A. Zinger, S. Soriano, G. Baudo, E. De Rosa, F. Taraballi, S. Villapol, Biomimetic nanoparticles as a theranostic tool for traumatic brain injury, Adv. Funct. Mater. 31 (2021), 2100722, https://doi.org/10.1002/adfm.202100722.
[45] J. Zhang, Y. Zheng, Y. Luo, Y. Du, X. Zhang, J. Fu, Curcumin inhibits LPS-induced neuroinflammation by promoting microglial M2 polarization via TREM2/TLR4/NF-κB pathways in BV2 cells, Mol. Immunol. 116 (2019) 29–37, https://doi.org/10.1016/j.molimm.2019.09.020.
[46] F. Kong, X. Jiang, R. Wang, S. Zhai, Y. Zhang, D. Wang, Forsythoside B attenuates memory impairment and neuroinflammation via inhibition on NF-kappaB signaling in Alzheimer's disease, J. Neuroinflammation 17 (2020) 305, https://doi.org/10.1186/s12974-020-01967-2.
[47] H. Akel, R. Ismail, I. Csóka, Progress and perspectives of brain-targeting lipid-based nanosystems via the nasal route in Alzheimer's disease, Eur. J. Pharm. Biopharm. 148 (2020) 38–53, https://doi.org/10.1016/j.ejpb.2019.12.014.
[48] T.d.B. C, A.C. Rios, T.F.R. Alves, F. Batain, K.M.M. Crescencio, L.J. Lopes, A. Zielińska, P. Severino, G.M. P, E.B. Souto, M.V. Chaud, Cachexia: pathophysiology and ghrelin liposomes for nose-to-brain delivery, Int. J. Mol. Sci. 21 (2020), https://doi.org/10.3390/ijms21175974.
[49] S. Becchi, A. Buson, B.W. Balleine, Inhibition of vascular adhesion protein 1 protects dopamine neurons from the effects of acute inflammation and restores habit learning in the striatum, J. Neuroinflammation 18 (2021) 233, https://doi.org/10.1186/s12974-021-02288-8.
[50] C. Da Ré, J.M. Souza, F. Fróes, J. Taday, J.P. Dos Santos, L. Rodrigues, P. Sesterheim, C.A. Gonçalves, M.C. Leite, Neuroinflammation induced by lipopolysaccharide leads to memory impairment and alterations in hippocampal leptin signaling, Behav. Brain Res. 379 (2020), 112360, https://doi.org/10.1016/j.bbr.2019.112360.
[51] S. Viana da Silva, M.G. Haberl, P. Zhang, P. Bethge, C. Lemos, N. Gonçalves, A. Gorlewicz, M. Malezieux, F.Q. Gonçalves, N. Grosjean, C. Blanchet, A. Frick, U. V. Nägerl, R.A. Cunha, C. Mulle, Early synaptic deficits in the APP/PS1 mouse model of Alzheimer's disease involve neuronal adenosine A2A receptors, Nat. Commun. 7 (2016), 11915, https://doi.org/10.1038/ncomms11915.
[52] N. Zhao, Q.W. Yan, J. Xia, X.L. Zhang, B.X. Li, L.Y. Yin, B. Xu, Treadmill exercise attenuates aβ-induced mitochondrial dysfunction and enhances mitophagy activity in APP/PS1 transgenic mice, Neurochem. Res. 45 (2020) 1202–1214, https://doi.org/10.1007/s11064-020-03003-4.
[53] A. Parikh, K. Kathawala, J. Li, C. Chen, Z. Shan, X. Cao, X.F. Zhou, S. Garg, Curcumin-loaded self-nanomicellizing solid dispersion system: part II: in vivo safety and efficacy assessment against behavior deficit in Alzheimer disease, Drug Deliv Transl Res 8 (2018) 1406–1420, https://doi.org/10.1007/s13346-018-0570-0.
[54] H. Zhang, Y. Su, Z. Sun, M. Chen, Y. Han, Y. Li, X. Dong, S. Ding, Z. Fang, W. Li, W. Li, Ginsenoside Rg1 alleviates Aβ deposition by inhibiting NADPH oxidase 2 activation in APP/PS1 mice, J Ginseng Res 45 (2021) 665–675, https://doi.org/10.1016/j.jgr.2021.03.003.
[55] H. Wang, J. Lv, N. Jiang, H. Huang, Q. Wang, X. Liu, Ginsenoside Re protects against chronic restraint stress-induced cognitive deficits through regulation of NLRP3 and Nrf2 pathways in mice, Phytother Res. (2021), https://doi.org/10.1002/ptr.6947.
[56] C.Z. Cai, X.X. Zhuang, Q. Zhu, M.Y. Wu, H. Su, X.J. Wang, A. Iyaswamy, Z. Yue, Q. Wang, B. Zhang, Y. Xue, J. Tan, M. Li, H. He, J.H. Lu, Enhancing autophagy maturation with CCZ1-Mon1A complex alleviates neuropathology and memory defects in Alzheimer disease models, Theranostics 12 (2022) 1738–1755, https://doi.org/10.7150/thno.64148.
[57] L. Qian, O. Rawashdeh, L. Kasas, M.R. Milne, N. Garner, K. Sankorrakul, N. Marks, M.W. Dean, P.R. Kim, A. Sharma, M.C. Bellingham, E.J. Coulson, Cholinergic basal forebrain degeneration due to sleep-disordered breathing exacerbates pathology in a mouse model of Alzheimer's disease, Nat. Commun. 13 (2022) 6543, https://doi.org/10.1038/s41467-022-33624-y.
[58] A. Muntsant, F. Jiménez-Altayó, L. Puertas-Umbert, E. Jiménez-Xarrie, E. Vila, L. Giménez-Llort, Sex-dependent end-of-life mental and vascular scenarios for compensatory mechanisms in mice with normal and AD-neurodegenerative aging, Biomedicines 9 (2021) 111, https://doi.org/10.3390/biomedicines9020111.
[59] D. Daugherty, J. Goldberg, W. Fischer, R. Dargusch, P. Maher, D. Schubert, A novel Alzheimer's disease drug candidate targeting inflammation and fatty acid metabolism, Alzheimer's Res. Ther. 9 (2017) 50, https://doi.org/10.1186/s13195-017-0277-3.
[60] M. Gulinello, M. Gertner, G. Mendoza, B.P. Schoenfeld, S. Oddo, F. LaFerla, C. H. Choi, S.M. McBride, D.S. Faber, Validation of a 2-day water maze protocol in mice, Behav. Brain Res. 196 (2009) 220–227, https://doi.org/10.1016/j.bbr.2008.09.002.
[61] F.E.K. Al-Khuzaie, O. Bayat, A.D. Duru, Diagnosis of alzheimer disease using 2D MRI slices by convolutional neural network, Appl. Bionics Biomech. 2021 (2021), 6690539, https://doi.org/10.1155/2021/6690539.
[62] L. Nadal, P. Coupé, C. Helmer, J.V. Manjon, H. Amieva, F. Tison, J.F. Dartigues, G. Catheline, V. Planche, Differential annualized rates of hippocampal subfields atrophy in aging and future Alzheimer's clinical syndrome, Neurobiol. Aging 90 (2020) 75–83, https://doi.org/10.1016/j.neurobiolaging.2020.01.011.
[63] P. Pais-Roldán, C. Mateo, W.J. Pan, B. Acland, D. Kleinfeld, L.H. Snyder, X. Yu, S. Keilholz, Contribution of animal models toward understanding resting state functional connectivity, Neuroimage 245 (2021), 118630, https://doi.org/10.1016/j.neuroimage.2021.118630.
[64] R. Ni, Magnetic resonance imaging in animal models of Alzheimer's disease amyloidosis, Int. J. Mol. Sci. 22 (2021), 12768, https://doi.org/10.3390/ijms222312768.

[65] N. El Tannir El Tayara, B. Delatour, C. Le Cudennec, M. Guégan, A. Volk, M. Dhenain, Age-related evolution of amyloid burden, iron load, and MR relaxation times in a transgenic mouse model of Alzheimer's disease, Neurobiol. Dis. 22 (2006) 199–208, https://doi.org/10.1016/j.nbd.2005.10.013.

[66] M.F. Falangola, V.V. Dyakin, S.P. Lee, A. Bogart, J.S. Babb, K. Duff, R. Nixon, J. A. Helpern, Quantitative MRI reveals aging-associated T2 changes in mouse models of Alzheimer's disease, NMR Biomed. 20 (2007) 343–351, https://doi.org/10.1002/nbm.1163.

[67] J.C. Magee, C. Grienberger, Synaptic plasticity forms and functions, Annu. Rev. Neurosci. 43 (2020) 95–117, https://doi.org/10.1146/annurev-neuro-090919-022842.

[68] Y. Jeong, H.Y. Cho, M. Kim, J.P. Oh, M.S. Kang, M. Yoo, H.S. Lee, J.H. Han, Synaptic plasticity-dependent competition rule influences memory formation, Nat. Commun. 12 (2021) 3915, https://doi.org/10.1038/s41467-021-24269-4.

[69] S. Gao, J. Lin, T. Wang, Y. Shen, Y. Li, W. Yang, K. Zhou, H. Hu, Qingxin kaiqiao fang ameliorates memory impairment and inhibits apoptosis in APP/PS1 double transgenic mice through the MAPK pathway, Drug Des. Dev. Ther. 13 (2019) 459–475, https://doi.org/10.2147/dddt.S188505.

[70] L. Yuan, S. Liu, X. Bai, Y. Gao, G. Liu, X. Wang, D. Liu, T. Li, A. Hao, Z. Wang, Oxytocin inhibits lipopolysaccharide-induced inflammation in microglial cells and attenuates microglial activation in lipopolysaccharide-treated mice, J. Neuroinflammation 13 (2016) 77, https://doi.org/10.1186/s12974-016-0541-7.

[71] J.D. Iroegbu, O.K. Ijomone, O.M. Femi-Akinlosotu, O.M. Ijomone, ERK/MAPK signalling in the developing brain: perturbations and consequences, Neurosci. Biobehav. Rev. 131 (2021) 792–805, https://doi.org/10.1016/j.neubiorev.2021.10.009.